Quantitative mapping of strain and displacement fields over HR-TEM and HR-STEM images of crystals with reference to a virtual lattice

Nikolay Cherkashin, A. Louiset, A. Chmielewski, D.J. Kim, C. Dubourdieu, S. Schamm-Chardon

Quantitative mapping of strain and displacement fields over HR-TEM and HR-STEM images of crystals with reference to a virtual lattice

N. Cherkashin[1*], A. Louiset[1], A. Chmielewski[1], D. J. Kim[2], C. Dubourdieu[2,3], S. Schamm-Chardon[1]

1- CEMES-CNRS and Université de Toulouse, 29 rue Jeanne Marvig, BP 94347, 31055 Toulouse Cedex 4, France
2- Helmholtz Zentrum Berlin für Materialien und Energie, Hahn Meitner Platz 1, 14109 Berlin, Germany
3- Freie Universität Berlin, Physical Chemistry, Arnimallee 22, 14195 Berlin, Germany

*Corresponding author email: nikolay.cherkashin@cemes.fr

Abstract: A method for the reciprocal space treatment of high-resolution transmission electron microscopy (HR-TEM) and high-resolution scanning transmission electron microscopy (HR-STEM) images has been developed. Named "Absolute strain" (AbStrain), it allows for quantification and mapping of interplanar distances and angles, displacement fields and strain tensor components with reference to a user-defined Bravais lattice and with their corrections from the image distortions specific to HR-TEM and HR-STEM imaging. We provide the corresponding mathematical formalism. AbStrain goes beyond the restriction of the existing method known as geometric phase analysis by enabling direct analysis of the area of interest without the need for reference lattice fringes of a similar crystal structure on the same field of view. In addition, for the case of a crystal composed of two or more types of atoms, each with its own sub-structure constraint, we developed a method named "Relative displacement" for extracting sub-lattice fringes associated to one type of atom and measuring atomic columns displacements associated to each sub-structure with reference to a Bravais lattice or to another sub-structure. The successful application of AbStrain and Relative displacement to HR-STEM images of functional oxide ferroelectric heterostructures is demonstrated.

1. INTRODUCTION

A large number of nanoobjects of different types (precipitates, nanocrystals, 3D islands and 2D layers) are widely used in modern microelectronics. For example, Si and Ge nanocrystals buried in the gate oxide of MOSFET transistors are promising candidates for the large-scale, low-power integration in non-volatile semiconductor nanomemories [1-3]. Metal Ag and Ag doped nanoparticles embedded into a dielectric matrix [4] or AsSb nanoinclusions buried in the low-temperature grown (Al,Ga)(As,Sb) semiconductor films [5] can be used to enhance and manipulate electromagnetic fields. The localization of electrons and holes within self-assembled epitaxial InGaAs quantum dots offers fascinating opportunities for both basic and applied research [6, 7]. Chemical composition, unit cell structure, and intrinsic strain all influence the optical and electrical properties of such nanostructures. As a result, such parameters should be assessed with subnanometer spatial resolution and high precision.

Complex oxides are attractive for integration as thin films or nanostructures on a Si substrate for application in nanoelectronics, communication devices, electromechanical systems, or sensors because of their ferroelectric and piezoelectric properties [8-10]. Such an epitaxial integration leads to the modification of various material properties. Strain and atomic displacements are particularly concerned because they alter spontaneous polarization and may result in the polarization reversal [11-13]. Complex oxides are made up of Oxygen and two or more types of atoms, each of which has its own crystal sub-structure strain. The sub-structures can be strained and/or shifted differently,

although sharing a common Bravais lattice [14, 15]. Thus, atomic displacements must be measured for each sub-structure individually and in relation to others.

Nowadays, aberration corrected high-resolution transmission electron microscopy (HR-TEM) and HR scanning TEM (HR-STEM) images are used to determine the displacement and strain tensor fields following two techniques, Peak Finding (PF) and Geometric Phase Analysis (GPA). These techniques are based on the space they work in, real or reciprocal, respectively. Historically, the first state-of-the-art proposal concerned the measurement of local displacements of atomic columns directly from HR-TEM images superimposing a reference lattice of fringes to the experimental one [16]. Later, the GPA method, based on Fourier transform of HR-TEM images, was developed [17]. Then, an alternative real space algorithm was proposed and presented as complementary to GPA [18].

The real space PF method is based on a Gaussian-like fitting over fringes associated to atomic columns and localization of intensity peaks. Recently, different software applications have been proposed to operate it [19-22]. When the motif of a crystal structure contains two or more types of atoms, they allow for a selection of sub-lattice fringes associated to each type of atoms and their corresponding separate treatment. This is the PF method's advantage.

To provide a reliable fit over an atomic columns' image, the latter has to be highly contrasted and represented by a large number of pixels (> 25). With a total number of pixels per image usually limited to 2k x 2k, such a requirement can be satisfied only for images taken at relatively high magnification, which provides only a small field of view (typically < 20 nm x 20 nm). This is the real space method's major flaw. In addition, in order to get a high contrast image, usually a stack of several images should be taken over the same sample area followed by alignment and averaging procedures [23, 24]. The resulting prolonged exposure to the electron beam amplifies the problems related to a likely existing sample drift and damaging.

The reciprocal space-based method, GPA of a HR-(S)TEM image, uses Fast Fourier Transform (FFT) for the analysis of geometric phases extracted by Inverse FFT (IFFT) from reciprocal vectors selected by reciprocal space masks [17]. The geometric phase is defined as $-2\pi \boldsymbol{g_n^0}(\boldsymbol{r_0}).\boldsymbol{u}(\boldsymbol{r})^{\boldsymbol{GPA}}$. Here, $\boldsymbol{g_n^0}(\boldsymbol{r_0})$ is the reciprocal vector of the lattice fringes measured in some user-chosen reference zone of the image and $\boldsymbol{u}(\boldsymbol{r})^{\boldsymbol{GPA}}$ is the displacement field quantified within the lattice fringes of interest with respect to such a reference lattice satisfying the condition $\boldsymbol{u}(\boldsymbol{r_0})^{\boldsymbol{GPA}} = \boldsymbol{0}$. When two geometric phases corresponding to two noncolinear reciprocal vectors $\boldsymbol{g_1^0}(\boldsymbol{r_0})$ and $\boldsymbol{g_2^0}(\boldsymbol{r_0})$ are extracted, such a displacement field can be reconstructed over the whole field of view. Strain tensor components are then obtained from the geometric phases by their derivation. According to its guiding principle, GPA demands that both the lattice of interest and a reference lattice exist in the same image. Such a requirement might not be always satisfied. This is the case when the crystal structure of interest is embedded within an amorphous matrix [1-4] or a matrix composed of strained crystal structures [5, 6]. This is the first restriction of GPA.

The second important constraint of GPA is the requirement for the reference crystal structure to be very similar to the one of interest. In other words, practically, the reciprocal spots corresponding to the lattice fringes of the reference area and the zone of interest should be very close to each other. If not, the reciprocal spot of the lattice of interest will be too shifted from the center of the reciprocal space mask which is centered around the reference spot [5]. As a result, IFFT will induce some distortions in the extracted displacement and strain fields that reduces the precision and accuracy of the method. At worst, the spot of lattice fringes of interest can be located outside the mask, which would prevent extracting any signal from the zone of interest.

Handling individually various sub-lattices is not possible with GPA, in contrast to PF. This prevents GPA from being applied to the analysis of polarization-linked relative atomic displacements in complex oxides and polar semiconductors.

With no need to fit, the GPA's advantage over PF is a far lighter requirement on atomic column contrast. For most analyses, one image is sufficient [25-27]. Another advantage is that an atomic column can be represented by a limited number of pixels (> 4) that allows a large field of view (> 100 nm x 100 nm) [27].

Based on such comparisons, it can be concluded that the reciprocal space approach would be preferable to the real space one if sub-lattice selection is made possible and the analysis of the crystal structure of interest can be done without the need for imaging of a similar undistorted reference crystal structure over the same field of view. In order to do this, one should be able to conduct direct measurements of the absolute, not relative, values of interplanar distances and angles in the image of the deformed structure. In order to get displacement and strain tensor fields, these values should be compared to some Bravais lattice.

For this, we have to get rid of the specific aberrations inherent to TEM and STEM imaging which always have an impact on the measured values of the interplanar distances and angles.

HR-TEM images are created under zone axis conditions as a result of interference of electron waves diffracted from multiple planes. The image of fringes is formed under simultaneous illumination of the whole field of view by a parallel electron beam. Such images are subjected to three types of distortions: 1) CCD camera distortions related to fiber packaging faults that vary over the field of view; 2) projection lens distortions varying over the field of view, and 3) image calibration which is constant over the field of view but varies with focus conditions and depends on magnification. Each of the aforementioned distortions induces up to 5% of false strain values into the real strain values, making it impossible to directly quantify infinitesimal strain. While CCD camera and projection lens distortions were found to be removed quite successfully [28], the third issue remained unsolved until recently [5, 29].

With the era of aberration-corrected microscopes, HR-STEM imaging became very popular because, as for HRTEM, it is possible to reach atomic resolution but also to visually distinguish between chemically different atomic columns. To form a HR-STEM image in zone axis conditions, the electron beam is focused to a tiny spot (< 1 Å in diameter), which scans the sample horizontally in one line, with a fixed displacement step, pixel by pixel, before flying back and restarting the fast scan over a line below. Due to electronics-related instabilities of the probe, sample drift and calibration issues, the coordinates of the pixels arranged in a square-like image matrix do not correspond exactly to the intended coordinates of the sample. As a consequence, the recorded image presents many distortions when compared to the real structure of the sample. In more details, there are four types of issues: 1) random jitter of the origin of each fast scanline with respect to the sample coordinates [30, 31]; 2) periodic change of the probe displacement step along the fast scan direction; 3) imprinting of not intended positions on the sample when sample drifts; 4) pixel calibration error. So far, the only approach which allows to correct for “jitter” effect and, only partially, for sample drift distortion is based on the correction of the image [31]. It requires a pair of 0° and 90° rotated images which are mathematically treated in order to form a single image with modified intensity distribution. This again doubles the time during which the sample is beam exposed. Moreover, the rest of the distortions remains not corrected.

Here, we propose a method, Absolute strain (AbStrain), which allows for quantification and mapping of interplanar distances and angles, displacement fields and strain tensor components

reconstructed with reference to a user-chosen Bravais lattice and finally all corrected from distortions. For this, a HR(S)TEM image can be used without the need for some reference fringes of a similar crystal structure over the same field of view. Instead, in order to correct for all distortions and to provide an absolute image calibration in the zone of interest, one can use an image of some other known but arbitrary crystal structure taken at the same conditions. As input data, AbStrain uses geometric phases extracted by GPA for a couple of reciprocal vectors present in a direct FFT of a zone of interest. Then, with AbStrain, we propose two approaches to determine the displacement field and strain tensor. The first approach provides the components of an absolute strain tensor with reference to a user-chosen Bravais lattice from which the displacement field is deduced. The second approach starts with the reconstruction of an absolute displacement field with reference to a Bravais lattice from which the strain tensor is deduced.

Moreover, we propose a method, Relative displacement, which allows to isolate individual images of sub-lattice fringes associated to different kinds of atoms and extract relative atomic displacements, which is important for the analysis of polarization-linked displacements in complex oxides and polar semiconductors.

In this paper, the mathematical formalism for the two AbStrain approaches is first described. Within each approach, the methods for absolute strain tensor, displacements, interplanar distances and angles correction from various distortions are presented specifically for HR-TEM and HR-STEM images. Then, we present the method which allows for the decomposition of a HR-STEM image of a crystal made up of two or more types of atoms into the individual images of the sub-lattice fringes associated to each type of atoms followed by the method for calculating the relative displacement field of shifted sub-structures with reference to some measured barycenter of one of the sub-structures.

Finally, we consider a practical application of AbStrain and Relative displacement to a Si (001)/a-SiO_x/$SrTiO_3$ (001)/$BaTiO_3$ (001) heterostructure.

2. MATHEMATICAL FORMALISM FOR ABSTRAIN

In general, we refer to a material as being strained when a portion of its continuum body has been modified from its initial shape due to the displacement of its constituent points. A crystalline structure (a lattice and a motif composed of one or several atoms) can be considered as a subset of the continuum body. The goal of AbStrain is to relate the atomic columns positions to the displacement and strain tensor components of a continuous body specified in user-chosen Cartesian coordinate system. Let us use the $\boldsymbol{yz}$ notation to define the natural coordinate system of vectors parallel to the horizontal and vertical axes in an image as displayed in the Digital Micrograph (DM) environment and the $\boldsymbol{y'z'}$ notation for an arbitrary oriented coordinate system (practically corresponding to some orthogonal directions related to the geometric configuration of the studied area of interest, for example, an interface). We place our approach in the approximation of infinitesimal strain theory, i.e., when small body shape changes are expected. As we deal with 2D images, we describe the 2D strain tensor, here in the $\boldsymbol{yz}$-plane. Within the first AbStrain approach, we deduce the components of an absolute strain tensor in terms of reciprocal vectors of the imaged and virtual unstrained structures. When to the second AbStrain approach, we describe a formalism for the transition from the imaged-to- virtual real structure reference, that provides a displacement field defined with reference to a user-chosen Bravais lattice.

2.1 First approach: Strain tensor and rigid body rotation in terms of reciprocal space vectors with reference to a user-chosen Bravais lattice

Real space - First, in the real space, we choose a reference square-like body cell with dimensions $dy \times dz$ and sides parallel to $\boldsymbol{y}$ and $\boldsymbol{z}$ axes (Fig. 1a, black line). When strained, the cell takes on a new shape with inside points being displaced by $\boldsymbol{u}(y,z)$ (Fig. 1a, red line). The vertex placed on the $\boldsymbol{y}$-axis is displaced in the $\boldsymbol{y}$ direction by a quantity $\frac{\partial u_y}{\partial y}dy$ and in the $\boldsymbol{z}$ direction by a quantity $\frac{\partial u_z}{\partial y}dy$. The displacements of a vertex located on the $\boldsymbol{z}$ -axis can be expressed simply by reversing the y and z indexes. The components of the infinitesimal strain tensor and rigid body rotation are then given

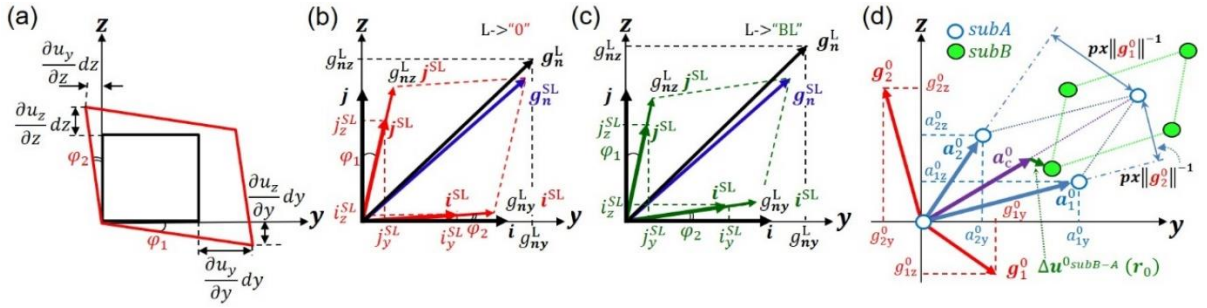

Fig. 1 Unstrained (black) and strained (red, green) continuum body cells represented in real space (a) and in reciprocal space (b), (c). Red unit cell vectors in (b) represent strain defined with reference to $\boldsymbol{g}_n^0$ reciprocal vectors (n = 1 and 2), measured by GPA in the reference zone. Green unit cell vectors in (c) represent strain defined with reference to $\boldsymbol{g}_n^{BL}$ reciprocal vectors (n=1 and 2) of the Bravais lattice of the material. Violet vectors in (b) and (c) indicate strained $\boldsymbol{g}_n^{SL}$ reciprocal vectors (n = 1 and 2) in the image; (d) Representation of atoms of two sub-structures (A: blue open circles, B: green filled circles) and the coordinates of subA cell (blue) in relation to $\boldsymbol{g}_1^0$ and $\boldsymbol{g}_2^0$ reciprocal vectors measured by GPA in the reference zone. The vectors $\boldsymbol{a}_c^0$ (violet) and $\Delta\boldsymbol{u}^{0subB-A}(\boldsymbol{r}_0)$ (green) indicate the barycenter within the atomic cell of subA and the displacement between the atoms of subB B relative to such a barycenter, respectively, within the reference zone.

by the expressions

$$\varepsilon_{yy} = \frac{\partial u_y}{\partial \mathrm{y}}, \varepsilon_{zz} = \frac{\partial u_z}{\partial \mathrm{z}}, \varepsilon_{yz} = \frac{1}{2}\left(\frac{\partial u_z}{\partial \mathrm{y}} + \frac{\partial u_y}{\partial \mathrm{z}}\right), \tag{1}$$

$$\omega_{yz} = \frac{1}{2}\left(\frac{\partial u_z}{\partial \mathrm{y}} - \frac{\partial u_y}{\partial \mathrm{z}}\right), \tag{2}$$

where ε_{yy} and ε_{zz} are the normal strain components in the $\boldsymbol{y}$ and $\boldsymbol{z}$ directions, ε_{yz} is the shear strain and ω_{yz} is rigid body rotation defined to be positive counterclockwise.

Strain tensor and rigid body rotation in reciprocal space - The real space cell changes can be expressed in the reciprocal space (more details can be found in [32]). The reference reciprocal space cell has the dimensions $\boldsymbol{i} \times \boldsymbol{j}$, where $\|\boldsymbol{i}\| = \|\boldsymbol{j}\| = 1$ in pixel units and sides $\boldsymbol{i}, \boldsymbol{j}$ are aligned along $\boldsymbol{y}$ and $\boldsymbol{z}$ axes (Fig. 1b, black vectors). When the real space cell is deformed, the reciprocal space cell changes accordingly. Its base vectors $\boldsymbol{i}^{SL}, \boldsymbol{j}^{SL}$ (Fig. 1b and c, red and green arrows, the superscript "*L*" stands for "lattice" as a reference, where L="0" when this reference is a zone in the image and L="BL" when this reference is a chosen Bravais lattice, "SL" stands for "strained" with reference to this "lattice") can be expressed in the $(\boldsymbol{i}, \boldsymbol{j})$ reference as

$$\boldsymbol{i}^{SL} = i_y^{SL}\boldsymbol{i} + i_z^{SL}\boldsymbol{j}, \tag{3}$$

$$\boldsymbol{j}^{SL} = j_y^{SL}\boldsymbol{i} + j_z^{SL}\boldsymbol{j}, \tag{4}$$

with $\|\boldsymbol{i}^{SL}\| = \sqrt{{i_y^{SL}}^2 + {i_z^{SL}}^2}$ and $\|\boldsymbol{j}^{S}\| = \sqrt{{j_y^{SL}}^2 + {j_z^{SL}}^2}$. All components of the strain tensor and rigid body rotation can be redefined in terms of reciprocal space vectors as

$$\varepsilon_{yy} = \frac{1}{\|\boldsymbol{i}^{SL}\|} - 1, \varepsilon_{zz} = \frac{1}{\|\boldsymbol{j}^{SL}\|} - 1, \varepsilon_{yz} = -\frac{1}{2}\left(\frac{i_z^{SL}}{i_y^{SL}} + \frac{j_y^{SL}}{j_z^{SL}}\right), \quad (5)$$

$$\omega_{yz} = -\frac{1}{2}\left(\frac{i_z^{SL}}{i_y^{SL}} - \frac{j_y^{SL}}{j_z^{SL}}\right). \quad (6)$$

In the reciprocal space, the coordinates of reciprocal vectors construct a discrete sub-set of the reciprocal continuum body. Let's consider a reference lattice to be characterized by 2 non-collinear reciprocal vectors $\boldsymbol{g}_n^L$. If GPA is applied (Fig. 1b, black arrow), the coordinates of such vectors, $\boldsymbol{g}_n^L = \boldsymbol{g}_n^0$ are measured in the reference zone of the image. If a Bravais lattice of the material is chosen as a reference (Fig. 1c, black arrow), the coordinates of such vectors, $\boldsymbol{g}_n^L = \boldsymbol{g}_n^{BL}$, characterized by different Miller indices $\{h_n, k_n, l_n\}$, lattice parameters $\{a_n, b_n, c_n\}$ and angles $\{\alpha_n, \beta_n, \gamma_n\}$, correspond to that of the *n*-th reciprocal structure vector of the unstrained material. When a reference lattice is transformed into the strained one, $\boldsymbol{g}_n^L$ transforms into the reciprocal vector $\boldsymbol{g}_n^{SL}$. The reciprocal vectors $\boldsymbol{g}_n^L$ and $\boldsymbol{g}_n^{SL}$ can be expressed in units of the $(\boldsymbol{i}^L = \boldsymbol{i}, \boldsymbol{j}^L = \boldsymbol{j})$ and $(\boldsymbol{i}^{SL}, \boldsymbol{j}^{SL})$ cells, respectively, as

$$\boldsymbol{g}_n^L = \mathrm{g}_{ny}^L \boldsymbol{i} + \mathrm{g}_{nz}^L \boldsymbol{j}, \quad (7)$$

$$\boldsymbol{g}_n^{SL} = \mathrm{g}_{ny}^L \boldsymbol{i}^{SL} + \mathrm{g}_{nz}^L \boldsymbol{j}^{SL}, \quad (8)$$

with $\left(\mathrm{g}_{ny}^L, \mathrm{g}_{nz}^L\right) \in \mathbb{R}^2$ being the coordinates of $\boldsymbol{g}_n^L$ **Erreur ! Source du renvoi introuvable.**(Fig. 1b).

From Eqs. (3-4) and Eqs. (7-8), the reciprocal vector $\boldsymbol{g}_n^{SL}$ can be expressed in units of the $(\boldsymbol{i}, \boldsymbol{j})$ cell as

$$\boldsymbol{g}_n^{SL} = \left(\mathrm{g}_{ny}^L i_y^{SL} + \mathrm{g}_{nz}^L j_y^{SL}\right)\boldsymbol{i} + \left(\mathrm{g}_{ny}^L i_z^{SL} + \mathrm{g}_{nz}^L j_z^{SL}\right)\boldsymbol{j}, \quad (9)$$

that gives for two non-collinear vectors $\boldsymbol{g}_1^{SL}$ and $\boldsymbol{g}_2^{SL}$

$$\mathrm{g}_{1y}^{SL} = \mathrm{g}_{1y}^L i_y^{SL} + \mathrm{g}_{1z}^L j_y^{SL}, \quad (10)$$

$$\mathrm{g}_{1z}^{SL} = \mathrm{g}_{1y}^L i_z^{SL} + \mathrm{g}_{1z}^L j_z^{SL}, \quad (11)$$

$$\mathrm{g}_{2y}^{SL} = \mathrm{g}_{2y}^L i_y^{SL} + \mathrm{g}_{2z}^L j_y^{SL}, \quad (12)$$

$$\mathrm{g}_{2z}^{SL} = \mathrm{g}_{2y}^L i_z^{SL} + \mathrm{g}_{2z}^L j_z^{SL}. \quad (13)$$

The system of these four Eqs. solved for $\left\{i_y^{SL}, i_z^{SL}, j_y^{SL}, j_z^{SL}\right\}$ yields

$$i_y^{SL} = \frac{\mathrm{g}_{1z}^L \mathrm{g}_{2y}^{SL} - \mathrm{g}_{2z}^L \mathrm{g}_{1y}^{SL}}{\mathrm{g}_{1z}^L \mathrm{g}_{2y}^L - \mathrm{g}_{1y}^L \mathrm{g}_{2z}^L}, \quad (14)$$

$$i_z^{SL} = \frac{\mathrm{g}_{1z}^L \mathrm{g}_{2z}^{SL} - \mathrm{g}_{2z}^L \mathrm{g}_{1z}^{SL}}{\mathrm{g}_{1z}^L \mathrm{g}_{2y}^L - \mathrm{g}_{1y}^L \mathrm{g}_{2z}^L}, \quad (15)$$

$$j_y^{SL} = \frac{\mathrm{g}_{2y}^L \mathrm{g}_{1y}^{SL} - \mathrm{g}_{1y}^L \mathrm{g}_{2y}^{SL}}{\mathrm{g}_{1z}^L \mathrm{g}_{2y}^L - \mathrm{g}_{1y}^L \mathrm{g}_{2z}^L}, \quad (16)$$

$$j_z^{SL} = \frac{\mathrm{g}_{2y}^L \mathrm{g}_{1z}^{SL} - \mathrm{g}_{1y}^L \mathrm{g}_{2z}^{SL}}{\mathrm{g}_{1z}^L \mathrm{g}_{2y}^L - \mathrm{g}_{1y}^L \mathrm{g}_{2z}^L}. \quad (17)$$

In practice, after a direct FFT of a zone of interest (ZOI), one should extract geometric phases and read the coordinates of the reference $\boldsymbol{g}_n^0$ vectors within the ZOI. By doing so, the reciprocal space mask utilized by GPA will be properly centered around the spots of the reciprocal vectors of the ZOI. In addition to not requiring any other *similar* reference structure over the field of view of the image, this will enable the preventing of IFFT distortions. The coordinates of the $\boldsymbol{g}_n^{SL}$ vectors can be calculated from the geometric phase images, $\partial\varphi_n$ corresponding to the reference $\boldsymbol{g}_n^0$ vectors as proposed by M. J. Hÿtch et al. [17]

$$\mathrm{g}_{ny}^{SL} = \mathrm{g}_{ny}^0 + \frac{1}{2\pi}\frac{\partial\varphi_n}{\partial y}, \quad (18)$$

$$g_{nz}^{SL} = g_{nz}^{0} + \frac{1}{2\pi}\frac{\partial \varphi_n}{\partial z}. \quad (19)$$

By substituting these values and $\boldsymbol{g}_n^0$ for $\boldsymbol{g}_n^L$ in Eq. (14-17), one gets the coordinates of the reciprocal unit cell ($\boldsymbol{i}^{SL}, \boldsymbol{j}^{SL}$) (L="0") deformed with reference to the reciprocal lattice of $\boldsymbol{g}_n^0$ vectors (Fig. 1b, red arrows). The latter, once substituted in Eqs. (5-6), provide the components of the strain tensor and rigid body rotation measured by GPA.

In the next step, the Bravais lattice vectors are to be substituted for $\boldsymbol{g}_n^L$ in Eqs. (14-17) (Fig. 1c, black arrow) that would provide the coordinates of the reciprocal unit cell ($\boldsymbol{i}^{SL}, \boldsymbol{j}^{SL}$) deformed with reference to the Bravais lattice (L= "BL") (Fig. 1c, green arrows). For this, one should choose the orientation of the Bravais lattice, characterized by such $\boldsymbol{g}_n^L$ vectors relative to the ***yz***- coordinate system. The coordinates of $\boldsymbol{g}_1^L$ and $\boldsymbol{g}_2^L$ vectors can be presented as

$$g_{1y}^{L} = px\|\boldsymbol{G}_1^L\|\cos\alpha, \quad (20)$$
$$g_{1z}^{L} = px\|\boldsymbol{G}_1^L\|\sin\alpha, \quad (21)$$
$$g_{2y}^{L} = px\|\boldsymbol{G}_2^L\|\cos(\alpha+\alpha_{12}), \quad (22)$$
$$g_{2z}^{L} = px\|\boldsymbol{G}_2^L\|\sin(\alpha+\alpha_{12}), \quad (23)$$

where α is an angle between $\boldsymbol{g}_1^L$ and $\boldsymbol{y}$-axis, α_{12} is an angle between $\boldsymbol{g}_1^L$ and $\boldsymbol{g}_2^L$, $\|\boldsymbol{G}_1^L\|$ and $\|\boldsymbol{G}_2^L\|$ are the lengths of the reciprocal vectors $\boldsymbol{g}_1^L$ and $\boldsymbol{g}_2^L$ of the virtual unstrained structure in absolute units (for example, in nm^{-1}) and px is the size of a pixel in the image in the inverse absolute units, i.e. in nm.

By substituting Eqs. (20-23) in Eqs. (14-17) one gets

$$i_y^{SL} = \frac{1}{px\sin\alpha_{12}}\left(-\frac{g_{2y}^{SL}\sin\alpha}{\|\boldsymbol{G}_2^L\|} + \frac{g_{1y}^{SL}\sin(\alpha+\alpha_{12})}{\|\boldsymbol{G}_1^L\|}\right), \quad (24)$$
$$i_z^{SL} = \frac{1}{px\sin\alpha_{12}}\left(-\frac{g_{2z}^{SL}\sin\alpha}{\|\boldsymbol{G}_2^L\|} + \frac{g_{1z}^{SL}\sin(\alpha+\alpha_{12})}{\|\boldsymbol{G}_1^L\|}\right), \quad (25)$$
$$j_y^{SL} = \frac{1}{px\sin\alpha_{12}}\left(\frac{g_{2y}^{SL}\cos\alpha}{\|\boldsymbol{G}_2^L\|} - \frac{g_{1y}^{SL}\cos(\alpha+\alpha_{12})}{\|\boldsymbol{G}_1^L\|}\right), \quad (26)$$
$$j_z^{SL} = \frac{1}{px\sin\alpha_{12}}\left(\frac{g_{2z}^{SL}\cos\alpha}{\|\boldsymbol{G}_2^L\|} - \frac{g_{1z}^{SL}\cos(\alpha+\alpha_{12})}{\|\boldsymbol{G}_1^L\|}\right). \quad (27)$$

$\|\boldsymbol{G}_1^L\|$, $\|\boldsymbol{G}_2^L\|$ and the angle α_{12} are calculated by using their crystallographic definitions as functions of the Bravais lattice parameters, angles and Miller indices. The angle α is linked to the rigid body rotation of the Bravais lattice with respect to the imaged structure and thus, any value may be chosen for it. However, to satisfy infinitesimal strain approximation, it is worthwhile to achieve a rigid body rotation that is close or equal to zero in the GPA reference zone. Such a condition yields

$$\frac{i_z^{SL}}{i_y^{SL}} - \frac{j_y^{SL}}{j_z^{SL}} = 0 \; for \; \boldsymbol{g}_n^{SL} = \boldsymbol{g}_n^0 . \quad (28)$$

When Eqs. (24-27) are substituted in Eq. (28), one gets an expression for α

$$\alpha = \frac{1}{2}\tan^{-1}\frac{2\|\boldsymbol{G}_2^L\|\sin\alpha_{12}\left(\|\boldsymbol{G}_1^L\|(g_{1y}^0 g_{2y}^0 - g_{1z}^0 g_{2z}^0) - \|\boldsymbol{G}_2^L\|\cos\alpha_{12}\left(g_{1y}^{0\,2} - g_{1z}^{0\,2}\right)\right)}{\|\boldsymbol{G}_1^L\|^2\left(g_{2y}^{0\,2} - g_{2z}^{0\,2}\right) - 2\|\boldsymbol{G}_1^L\|\|\boldsymbol{G}_2^L\|\cos\alpha_{12}\left(g_{1y}^0 g_{2y}^0 - g_{1z}^0 g_{2z}^0\right) + \|\boldsymbol{G}_2^L\|^2\cos(2\alpha_{12})\left(g_{1y}^{0\,2} - g_{1z}^{0\,2}\right)}, \; L = \text{“}BL\text{”} \quad (29)$$

Such a value of α can be substituted in Eqs. (24-27) to calculate $\left\{i_y^{SL}, i_z^{SL}, j_y^{SL}, j_z^{SL}\right\}$. Finally, these values can be substituted in Eqs. (5-6) to calculate strain tensor components and rigid body rotation maps with reference to the Bravais lattice.

An example of application of such an approach is shown in Fig. 2(a-c) and its validation in Fig. 2(d-f). This is a practical case of a cross-sectional (1-10) HR-TEM image of Si (Fig. 2(a)).

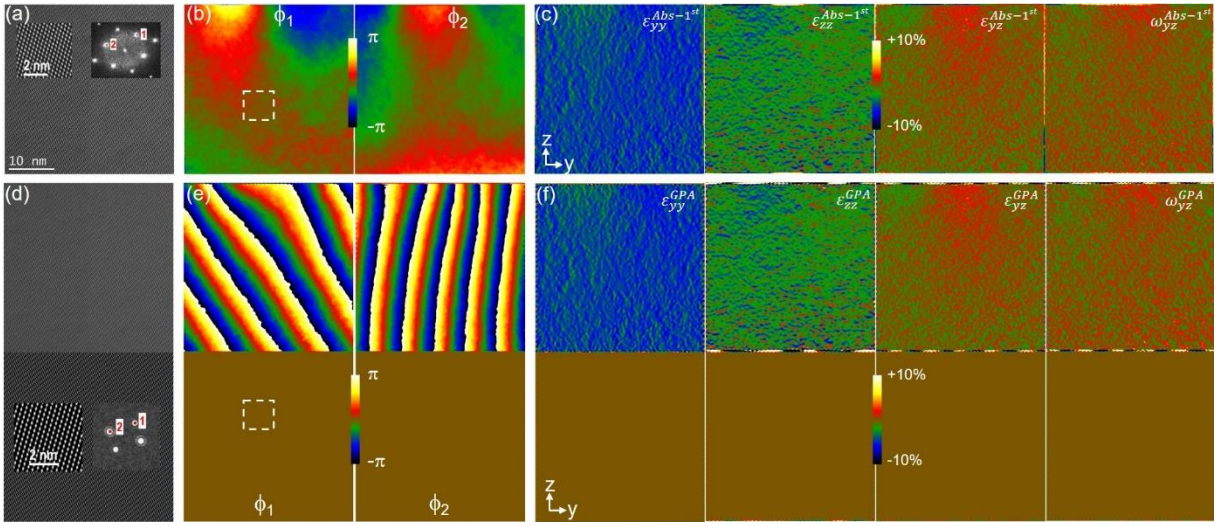

*Fig. 2 (a) Cross-sectional (1-10) HR-TEM image of Si; (b) Geometric phases extracted by GPA with $\boldsymbol{g}_1^0$ and $\boldsymbol{g}_2^0$ (selected diffraction spots 1 and 2 are shown in (a) in the inserted FFT); (c) Strain tensor and rigid body rotation obtained by AbStrain-1st for **yz**-coordinate system with reference to the Bravais lattice of Si structure; (d) Image constructed with two parts : on top, from the experimental HR-TEM image of Si and on bottom, from a simulated image consisting of cosine like fringes with the distance and angles corresponding to {111} planes of Si structure; (e) Geometric phases extracted by GPA with reference to the simulated part of the image (d); (f) Strain tensor and rigid body rotation obtained by GPA.*

Two reciprocal vectors used for GPA's extraction of the corresponding geometric phases are noted in the FFT of the image presented in insert (Fig. 2(a)). After reading the $\boldsymbol{g}_1^0$ and $\boldsymbol{g}_2^0$ coordinates within the reference zone of GPA (see white rectangle in Fig.2(b)) and assigning those vectors to $\boldsymbol{G}_1^{BL} = {[111]}/{a^{Si}}$ and $\boldsymbol{G}_2^{BL} = {[\bar{1}\bar{1}1]}/{a^{Si}}$ of Si lattice with $a^{Si} = 0.5431nm$, the first AbStrain approach provides the strain tensor and rigid body rotation with reference to the Bravais lattice of Si structure (Fig. 2(c)). Note a strong variation of all the components over the field of view and a significant relative difference between the values of the normal strain components. For comparison, we have simulated an image consisting of cosine like fringes with the distance and angles corresponding to $\boldsymbol{G}_1^{BL} = {[111]}/{a^{Si}}$ and $\boldsymbol{G}_2^{BL} = {[\bar{1}\bar{1}1]}/{a^{Si}}$. The image was simulated beneath the experimental one (Fig. 2(d)). By using the simulated image like a reference for GPA phases (Fig. 2(e)), the corresponding strain tensor and rigid body rotation were obtained by GPA (Fig. 2(f)). A one-to-one agreement between Fig. 2(c) and Fig. 2(f) indicates the validity of the AbStrain-1st method.

Since the Si structure was a priori unstrained, all these components arise from CCD camera, projections lens and pixel calibration error distortions. When a crystal structure of interest is imaged at the same conditions, absolute strain tensor and rigid body rotation maps obtained by AbStrain-1st with reference to the corresponding Bravais lattice can be corrected by a subtraction of those obtained for Si, like was demonstrated in our several works [5, 29, 33].

2.2 First approach: Displacement field with reference to a user-chosen Bravais lattice

Displacement field with reference to a user-chosen Bravais lattice, $\{\boldsymbol{u}_y^{SL}, \boldsymbol{u}_z^{SL}\}$ (L= "BL") can be determined from the previously calculated strain tensor components and rigid body rotation by their integration following the definitions

$$\int_{z_0}^{z} \frac{\partial u_y^{SL}(y,z')}{\partial z'}\, dz' = u_y^{SL}(y,z) - u_y^{SL}(y,z_0), \tag{30}$$

$$\int_{y_0}^{y} \frac{\partial u_y^{SL}(y',z)}{\partial y'}\, dy' = u_y^{SL}(y,z) - u_y^{SL}(y_0,z). \tag{31}$$

$$\int_{y_0}^{y} \frac{\partial u_z^{SL}(y',z)}{\partial y'}\, dy' = u_z^{SL}(y,z) - u_z^{SL}(y_0,z), \tag{32}$$

$$\int_{z_0}^{z} \frac{\partial u_z^{SL}(y,z')}{\partial z'}\, dz' = u_z^{SL}(y,z) - u_z^{SL}(y,z_0), \tag{33}$$

where (y_0, z_0) is the starting point (for example, left bottom corner of the DM image) for integration satisfying the boundary condition $u_y^{SL}(y_0,z_0) = u_z^{SL}(y_0,z_0) = 0$. We get from Eqs. (30-33)

$$\int_{z_0}^{z} \frac{\partial u_y^{SL}(y,z')}{\partial z'}\, dz' \Bigg|_{y=y_0} = u_y^{SL}(y_0,z), \tag{34}$$

$$\int_{y_0}^{y} \frac{\partial u_y^{SL}(y',z)}{\partial y'}\, dy' \Bigg|_{z=z_0} = u_y^{SL}(y,z_0), \tag{35}$$

$$\int_{y_0}^{y} \frac{\partial u_z^{SL}(y',z)}{\partial y'}\, dy' \Bigg|_{z=z_0} = u_z^{SL}(y,z_0), \tag{36}$$

$$\int_{z_0}^{z} \frac{\partial u_z^{SL}(y,z')}{\partial z'}\, dz' \Bigg|_{y=y_0} = u_z^{SL}(y_0,z), \tag{37}$$

that yields

$$\begin{aligned} u_y^{SL}(y,z) &= \int_{z_0}^{z} \frac{\partial u_y^{SL}(y_0,z')}{\partial z'}\, dz' + \int_{y_0}^{y} \frac{\partial u_y^{SL}(y',z)}{\partial y'}\, dy' \\ &= \int_{z_0}^{z} \Big(\varepsilon_{yz}(y_0,z') - \omega_{yz}(y_0,z')\Big)\, dz' + \int_{y_0}^{y} \varepsilon_{yy}(y',z)\, dy', \end{aligned} \tag{38}$$

$$\begin{aligned} u_z^{SL}(y,z) &= \int_{y_0}^{y} \frac{\partial u_z^{SL}(y',z_0)}{\partial y'}\, dy' + \int_{z_0}^{z} \frac{\partial u_z^{SL}(y,z')}{\partial z'}\, dz' \\ &= \int_{y_0}^{y} \Big(\varepsilon_{yz}(y',z_0) + \omega_{yz}(y',z_0)\Big)\, dy' + \int_{z_0}^{z} \varepsilon_{zz}(y,z')\, dz'. \end{aligned} \tag{39}$$

Alternatively, one can obtain the same result by changing the paths of integration

$$u_y^{SL}(y,z) = \int_{y_0}^{y} \varepsilon_{yy}(y',z_0)\, dy' + \int_{z_0}^{z} \Big(\varepsilon_{yz}(y,z') - \omega_{yz}(y,z')\Big)\, dz', \tag{40}$$

$$u_z^{SL}(y,z) = \int_{z_0}^{z} \varepsilon_{zz}(y_0,z')\, dz' + \int_{y_0}^{y} \Big(\varepsilon_{yz}(y',z) + \omega_{yz}(y',z)\Big)\, dy'. \tag{41}$$

It is easy to verify that a partial derivation of Eqs. (38-39) and Eqs. (40-41) by corresponding y and z coordinates (Eqs. (1-2)) provides the components of the initial strain tensor.

Figure 3(a) shows the displacement field components obtained by application of this method to the maps of absolute strain tensor and rigid body rotation presented in Fig. 2(c). In order to avoid the contribution of the IFFT artifacts present at the edges of the image, the integration was realized with an indent of 40 pixels from all edges that slightly decreases the field of view.

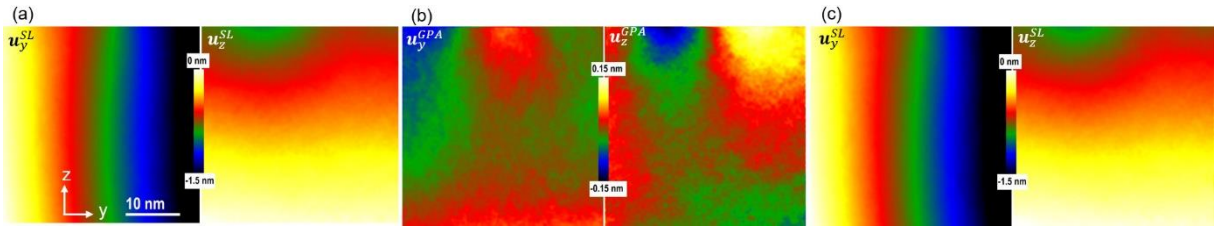

Fig. 3 Displacement field obtained from cross-sectional (1-10) HR-TEM image of Si using different approaches: (a) by AbStrain-1st with reference to the Si Bravais lattice through integration of absolute strain and rigid body rotation maps shown in Fig. 2(c); (b) by GPA with reference to $\boldsymbol{g_n^0(r_0)}$ *with* $\boldsymbol{r_0}$ *chosen in the middle of the image; (c) by AbStrain-2nd with reference to the Si Bravais lattice modifying* $\{\boldsymbol{u_y^{GPA}}, \boldsymbol{u_z^{GPA}}\}$ *of (b) with linear displacement field* $\boldsymbol{u^0}$ *calculated by AbStrain-1st ensuring a transition from* $\boldsymbol{g_n^0(r_0)}$ *to* $\boldsymbol{g_n^L}$ *of the Si Bravais lattice .*

In order that such a method for calculation of $\{\boldsymbol{u_y^{SL}}, \boldsymbol{u_z^{SL}}\}$ works properly, the integration must be done over a rectangular like area of the crystal along ***y*** and ***z*** axes. If the area comprises amorphous regions, the noise integrated over those areas will affect the values determined in the crystalline parts of the image. Thus, its application is quite limited when amorphous regions are mixed with some crystalline ones over a field of view of an arbitrary HR image. Our second approach, which will be presented later, does not have such a limitation.

2.3 First approach: Correction for distortions of strain tensor, rigid body rotation with reference to a virtual unstrained structure and interplanar distances

As already introduced, atomic structure images are subjected to distortions related to aberrations inherent to the used imaging mode, TEM or STEM. Since HR-TEM and HR-STEM images are differently distorted, the extracted images of absolute strain and displacement fields should be corrected accordingly.

HR-TEM image - Any two HR-TEM images taken at the same magnification and the same focus conditions are subjected to the same set of different distortions induced by a CDD camera, the image projection lens [28] and the pixel calibration error. Except for the latter distortion, the others vary over the field of view. Thus, the data extracted from the reference HR-TEM image of known unstrained structure (Fig. 2(c)) can be used for correction of that of the HR-TEM image of interest. For this, by using the same field of view in both images, the maps of strain tensor components and rigid body rotation extracted with reference to a Bravais lattice of the unstrained crystal have to be subtracted from the maps of strain tensor and rigid body rotation extracted with reference to corresponding Bravais lattice of the strained structure of interest.

Let's consider two different structures L_1 and L_2 of known Bravais lattices and compositions. Let's assume that we have a HR image of unstrained L_1 and a HR image of strained L_2. Both images are assumed to be taken at the same conditions and subjected to the same distortions. By applying the AbStrain-1st procedure for both images, $\{i_y^{SL_1}, i_z^{SL_1}, j_y^{SL_1}, j_z^{SL_1}\}$ and $\{i_y^{SL_2}, i_z^{SL_2}, j_y^{SL_2}, j_z^{SL_2}\}$ then strain tensor and rigid body rotation components with reference to corresponding Bravais lattices can be mapped for each image.

The first structure being unstrained, any strain component extracted over its image with reference to its Bravais lattice would correspond to the image distortions which can be presented by the distortion's displacement field $\boldsymbol{u^{SL_1}}$. The same distortions are present in the image of the strained structure. Since displacement fields are additive variables, the displacement field in this second image

can be presented as $\boldsymbol{u}^{SL_2} = \boldsymbol{u}^{SL_{2corr}} + \boldsymbol{u}^{SL_1}$ where $\boldsymbol{u}^{SL_{2corr}}$ is the displacement field filtered from distortions which exists in the second structure. Strain components, which by definition are obtained by partial derivation of the displacement field (see Eqs. (1-2)), remain additive values as well. Thus, the correction of the values of strain components measured in the image of L_2 can be obtained by a subtraction of the distortion's strain components measured in the image of L_1

$$\varepsilon_{yy}^{corr} = \frac{1}{\|\boldsymbol{i}^{SL_2}\|} - \frac{1}{\|\boldsymbol{i}^{SL_1}\|}, \tag{42}$$

$$\varepsilon_{zz}^{corr} = \frac{1}{\|\boldsymbol{j}^{SL_2}\|} - \frac{1}{\|\boldsymbol{j}^{SL_1}\|}, \tag{43}$$

$$\varepsilon_{yz}^{corr} = -\frac{1}{2}\left(\left(\frac{i_z^{SL_2}}{i_y^{SL_2}} + \frac{j_y^{SL_2}}{j_z^{SL_2}}\right) - \left(\frac{i_z^{SL_1}}{i_y^{SL_1}} + \frac{j_y^{SL_1}}{j_z^{SL_1}}\right)\right), \tag{44}$$

$$\omega_{yz}^{corr} = -\frac{1}{2}\left(\left(\frac{i_z^{SL_2}}{i_y^{SL_2}} - \frac{j_y^{SL_2}}{j_z^{SL_2}}\right) - \left(\frac{i_z^{SL_1}}{i_y^{SL_1}} - \frac{j_y^{SL_1}}{j_z^{SL_1}}\right)\right). \tag{45}$$

When one is interested in the values of interplanar distances and angles corrected from distortions, they can be calculated as

$$d_1^{SL_{2corr}} = \frac{px}{\left\|\boldsymbol{g}_1^{SL_{2corr}}\right\|} = \frac{px}{\sqrt{g_{1y}^{SL_{2corr}\,2} + g_{1z}^{SL_{2corr}\,2}}}, \tag{46}$$

$$d_2^{SL_{2corr}} = \frac{px}{\left\|\boldsymbol{g}_2^{SL_{2corr}}\right\|} = \frac{px}{\sqrt{g_{2y}^{SL_{2corr}\,2} + g_{2z}^{SL_{2corr}\,2}}}, \tag{47}$$

$$\alpha_{12}^{SL_{2corr}} = \cos^{-1}\frac{g_{1y}^{SL_{2corr}} g_{2y}^{SL_{2corr}} + g_{1z}^{SL_{2corr}} g_{2z}^{SL_{2corr}}}{\sqrt{g_{1y}^{SL_{2corr}\,2} + g_{1z}^{SL_{2corr}\,2}}\sqrt{g_{2y}^{SL_{2corr}\,2} + g_{2z}^{SL_{2corr}\,2}}}, \tag{48}$$

where the corrected values of the coordinates of reciprocal vectors are given by

$$g_{ny}^{SL_{2corr}} = g_{ny}^{L_2} i_y^{SL_{2corr}} + g_{nz}^{L_2} j_y^{SL_{2corr}}, \tag{49}$$

$$g_{nz}^{SL_{2corr}} = g_{ny}^{L_2} i_z^{SL_{2corr}} + g_{nz}^{L_2} j_z^{SL_{2corr}}. \tag{50}$$

The $\left\{i_y^{SL_{2corr}}, j_y^{SL_{2corr}}, i_z^{SL_{2corr}}, j_z^{SL_{2corr}}\right\}$ can be calculated from a system of Eqs.

$$\frac{1}{\|\boldsymbol{i}^{SL_{2corr}}\|} = \frac{1}{\|\boldsymbol{i}^{SL_2}\|} - \frac{1}{\|\boldsymbol{i}^{SL_1}\|}, \tag{51}$$

$$\frac{1}{\|\boldsymbol{j}^{SL_{2corr}}\|} = \frac{1}{\|\boldsymbol{j}^{SL_2}\|} - \frac{1}{\|\boldsymbol{j}^{SL_1}\|}, \tag{52}$$

$$\frac{i_z^{SL_{2corr}}}{i_y^{SL_{2corr}}} + \frac{j_y^{SL_{2corr}}}{j_z^{SL_{2corr}}} = \left(\frac{i_z^{SL_2}}{i_y^{SL_2}} + \frac{j_y^{SL_2}}{j_z^{SL_2}}\right) - \left(\frac{i_z^{SL_1}}{i_y^{SL_1}} + \frac{j_y^{SL_1}}{j_z^{SL_1}}\right), \tag{53}$$

$$\frac{i_z^{SL_{2corr}}}{i_y^{SL_{2corr}}} - \frac{j_y^{SL_{2corr}}}{j_z^{SL_{2corr}}} = \left(\frac{i_z^{SL_2}}{i_y^{SL_2}} - \frac{j_y^{SL_2}}{j_z^{SL_2}}\right) - \left(\frac{i_z^{SL_1}}{i_y^{SL_1}} - \frac{j_y^{SL_1}}{j_z^{SL_1}}\right), \tag{54}$$

that yields

$$i_y^{SL_{2corr}} = \frac{1}{\left(\frac{1}{\|\boldsymbol{i}^{SL_2}\|} - \frac{1}{\|\boldsymbol{i}^{SL_1}\|}\right)\sqrt{\left(\frac{i_z^{SL_2}}{i_y^{SL_2}} - \frac{i_z^{SL_1}}{i_y^{SL_1}}\right)^2 + 1}}, \tag{55}$$

$$i_z^{SL_2corr} = \frac{\left(\frac{i_z^{SL_2}}{i_y^{SL_2}} - \frac{i_z^{SL_1}}{i_y^{SL_1}}\right)}{\left(\frac{1}{\|\boldsymbol{i}^{SL_2}\|} - \frac{1}{\|\boldsymbol{i}^{SL_1}\|}\right)\sqrt{\left(\frac{i_z^{SL_2}}{i_y^{SL_2}} - \frac{i_z^{SL_1}}{i_y^{SL_1}}\right)^2 + 1}}, \tag{56}$$

$$j_y^{SL_2corr} = \frac{\left(\frac{j_y^{SL_2}}{j_z^{SL_2}} - \frac{j_y^{SL_1}}{j_z^{SL_1}}\right)}{\left(\frac{1}{\|\boldsymbol{j}^{SL_2}\|} - \frac{1}{\|\boldsymbol{j}^{SL_1}\|}\right)\sqrt{\left(\frac{j_y^{SL_2}}{j_z^{SL_2}} - \frac{j_y^{SL_1}}{j_z^{SL_1}}\right)^2 + 1}}, \tag{57}$$

$$j_z^{SL_2corr} = \frac{1}{\left(\frac{1}{\|\boldsymbol{j}^{SL_2}\|} - \frac{1}{\|\boldsymbol{j}^{SL_1}\|}\right)\sqrt{\left(\frac{j_y^{SL_2}}{j_z^{SL_2}} - \frac{j_y^{SL_1}}{j_z^{SL_1}}\right)^2 + 1}}, \tag{58}$$

By substituting Eqs. (55-58) in Eqs. (49-50) and the latter in Eqs. (46-48), the maps of interplanar distances and angles in the strained structure corrected from the distortions can be extracted.

HR-STEM image – Any two HR-STEM images taken at the same magnification with the same sample drift are subjected to the same set of sample drift and pixel calibration error distortions. However, these images will always differ by scan distortions. Thus, for correction, unlike sample drift and pixel calibration errors, scan distortions present in one HR-STEM image cannot be quantified by using another HR-STEM image. We propose some alternative solutions.

Even though the scan distortions do not repeat over different images, any line of pixels acquired along the fast scan direction is almost not affected by such a distortion. This implies that the projection of any reciprocal vector on the scan direction is unaffected. Let's consider two cross-sectional (1-10) HR-STEM HAADF images of Si structure of the same field of view with orthogonal scan directions, further on referred to as 0° and 90° images, respectively (Fig. 4(a)). In practice, the scan direction is always horizontal, i.e. parallel to the y-axis. After acquiring the 0° image, the 90° image is obtained by imaging the same field of view rotated by 90°. The acquired image should then be rotated back by 90° and aligned with the 0° image. Afterwards, the maps of $g_{ny}^{SL} = g_{ny}^{O^\circ}$, $g_{nz}^{SL} = g_{nz}^{O^\circ}$ (Fig. 4(b)) and $g_{ny}^{SL} = g_{ny}^{9O^\circ}$, $g_{nz}^{SL} = g_{nz}^{9O^\circ}$ (Fig. 4(c)) are extracted from the corresponding images by using Eqs. (18-19).

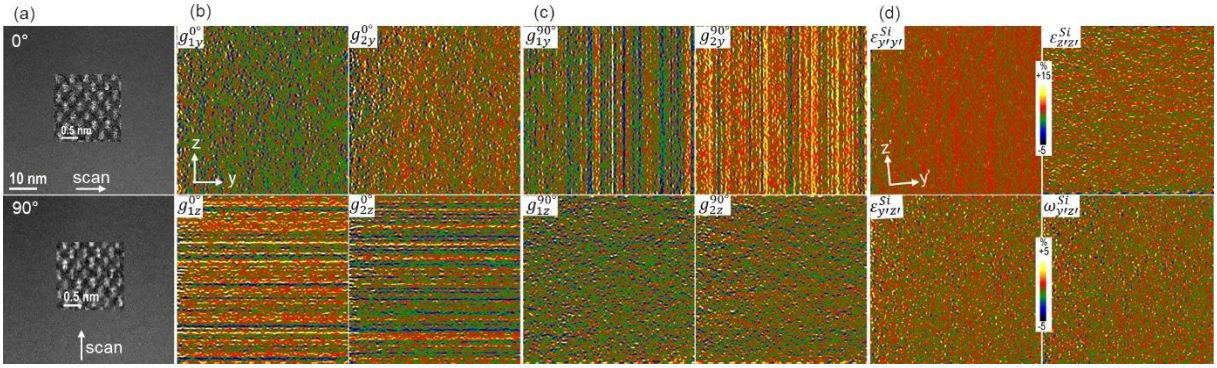

*Fig. 4 Application of AbStrain-1st to a couple of 0° and 90° HR-STEM images: (a) 0° and 90° cross-sectional (1-10) HR-STEM HAADF images of Si; (b) coordinates of $\boldsymbol{g}_1^{0^\circ}$ and $\boldsymbol{g}_2^{0^\circ}$ of 0° HR-STEM HAADF image; (c) coordinates of $\boldsymbol{g}_1^{90^\circ}$ and $\boldsymbol{g}_2^{90^\circ}$ of 90° HR-STEM HAADF image; (d) maps of absolute strain tensor and rigid body rotation obtained by AbStrain-1st with reference to the Si Bravais lattice in **y'z'**-coordinate system using a combination of $g_{ny}^{O^\circ}$ and $g_{nz}^{90^\circ}$, free of scan distortions.*

The projections of reciprocal vectors of the 0° image on the *y*-axis (Fig. 4(b), top) and that of the 90° image on the z-axis (Fig. 4(c), bottom) are unaffected by scan distortions. Thus, they can be combined as if they were from a single image. Further on, the $\{i_y^{0^\circ}, i_z^{90^\circ}, j_y^{0^\circ}, j_z^{90^\circ}\}$ are calculated by using Eqs. (24-29) and, finally, a strain tensor and rigid body rotation free of scan distortions with reference to the corresponding Bravais lattice is deduced for a desired y'z'-coordinate system (Fig. 4(d)). Such a tensor contains the residual distortions related to a sample drift and pixel calibration error.

The same procedure should be repeated over a couple of 0° and 90° HR-STEM images of the structure of interest taken shortly after or just before acquisition of the reference images of known unstrained structure, like Si here. Finally, the subtraction of the distortions measured over Si structure (Fig. 4(d)) from the strain tensor and rigid body rotation obtained with reference to a Bravais lattice of the structure of interest will provide the latter correction from all the distortions (Eqs. (42-45)).

2.4 Second approach: Displacement field with reference to a user-chosen Bravais lattice

The second approach implies first a calculation of the displacement field with reference to a user-chosen Bravais lattice, then of the absolute strain tensor and interplanar distances.

To begin, one should extract by GPA a displacement field $\boldsymbol{u}^{GPA} \equiv \boldsymbol{u}^{GPA}(\boldsymbol{r})$ from two geometric phase images $-2\pi \boldsymbol{g}_n^0(\boldsymbol{r}_0).\boldsymbol{u}^{GPA}$ satisfying the condition $\boldsymbol{u}^{GPA}(\boldsymbol{r}_0) = 0$ (Fig. 3(b)). Here, the reference lattice is considered to be composed of fringes of constant periodicities and orientations corresponding to the $\boldsymbol{g}_n^0(\boldsymbol{r}_0)$ vectors in the reciprocal space. The displacement field with reference to a Bravais lattice can be expressed as

$$\boldsymbol{u}^{SL} = \boldsymbol{u}^{GPA} + \boldsymbol{u}^0, \tag{59}$$

where $\boldsymbol{u}^0$ is the displacement field within the structure characterized by $\boldsymbol{g}_n^0(\boldsymbol{r}_0)$ vectors when referred to the Bravais lattice characterized by reciprocal vectors $\boldsymbol{g}_n^L$ (L= "BL"). The components of $\boldsymbol{u}^0$ are calculated as

$$\boldsymbol{u}_y^0 = px\left(\left(\varepsilon_{yz}^0 - \omega_{yz}^0\right)(i_0^{row} - i^{row}) + \varepsilon_{yy}^0(i^{col} - i_0^{col})\right), \tag{60}$$

$$\boldsymbol{u}_z^0 = px\left(\left(\varepsilon_{yz}^0 + \omega_{yz}^0\right)(i^{col} - i_0^{col}) + \varepsilon_{zz}^0(i_0^{row} - i^{row})\right), \tag{61}$$

where constant values of absolute strain tensor components ε_{ij}^0 and rigid body rotation ω_{yz}^0 are calculated from Eqs. (5-6) following the previously described formalism of AbStrain-1st by substituting the values provided by GPA of $\boldsymbol{g_n^0}$ for $\boldsymbol{g}_n^{SL}$ in Eqs. (24-29). Here, $\left(i^{col}, i^{row}\right)$ and $\left(i_0^{col}, i_0^{row}\right)$ define the coordinates of the pixel in integer units and that of the coordinate system origin within the reference zone, respectively. Coordinates $\left(i^{col}, i^{row}\right)$ are assigned to start with $(0,0)$ values in the left upper corner of the image, like defined in Digital Micrograph, Gatan software. Figure 3(c) demonstrates the application of AbStrain-2nd to the HR-TEM cross-sectional (1-10) image of Si structure shown in Fig. 2(a). Here, displacement field extracted by GPA with reference to $\boldsymbol{g_n^0}(\boldsymbol{r_0})$ (Fig. 3(b)) was modified by linear displacement field $\boldsymbol{u}^0$calculated by AbStrain-1st (Eqs. (60-61)) ensuring a transition from $\boldsymbol{g_n^0}(\boldsymbol{r_0})$ to $\boldsymbol{g_n^L}$ of the Si Bravais lattice.

Note a one-to-one agreement with the previously found absolute displacement field obtained within the AbStrain-1st by integration of absolute strain tensor and rigid body rotation maps (Fig. 3(a)), that confirms the reliability of both approaches. AbStrain-2nd is however preferable to use than AbStrain-1st when displacement field in a structure, which contain defects and amorphous areas over the field of view of the image, is of interest.

2.5 Second approach: Strain tensor, rigid body rotation with reference to a user-defined Bravais lattice and interplanar distances

While the displacement field with reference to a user-defined Bravais lattice has been determined, the absolute strain tensor and rigid body rotation maps can be obtained by their partial derivation (Eqs. (1-2)). The interplanar distances and angles can be further calculated by a pixel-by-pixel reconstruction of reciprocal vectors coordinates from corresponding strain tensor and rigid body rotation values and their substitution in Eqs. (46-48).

2.6 Second approach: Correction for distortions of displacement field defined with reference to a user-defined Bravais lattice

The subtraction of the displacement field measured over reference structure (Fig. 3(c)) from the displacement field obtained with reference to a Bravais lattice of the structure of interest will provide the latter correction from all the distortions. This is always true for HR-TEM images. For HR-STEM images, however, as scan distortions differ from one image to another, the simple subtraction of displacement fields would not provide a full correction of the absolute displacement within the ZOI. Therefore, in some cases, AbStrain-1st and the integration procedure have to be applied without alternative. The particular cases when AbStrain-2nd is still applicable for the analysis of HR-STEM images will be considered below.

HR-TEM image - As for correction of absolute strain tensor extracted from HR-TEM images, displacement field $\boldsymbol{u}^{SL_2}$ in structure of interest L_2 can be corrected from distortions by a subtraction of displacement field $\boldsymbol{u}^{SL_1}$ obtained in reference structure L_1 that gives for the corrected components

$$u_y^{SL_{2corr}} = u_y^{GPA_2} - u_y^{GPA_1} + px\left(\left(\varepsilon_{yz}^{0_2} - \varepsilon_{yz}^{0_1} + \omega_{yz}^{0_1} - \omega_{yz}^{0_2}\right)\left(i_0^{row} - i^{row}\right) + \left(\varepsilon_{yy}^{0_2} - \varepsilon_{yy}^{0_1}\right)\left(i^{col} - i_0^{col}\right)\right), \quad (62)$$

$$u_z^{SL_{2corr}} = u_z^{GPA_2} - u_z^{GPA_1} + px\left(\left(\varepsilon_{yz}^{0_2} - \varepsilon_{yz}^{0_1} + \omega_{yz}^{0_2} - \omega_{yz}^{0_1}\right)\left(i^{col} - i_0^{col}\right) + \left(\varepsilon_{zz}^{0_2} - \varepsilon_{zz}^{0_1}\right)\left(i_0^{row} - i^{row}\right)\right). \quad (63)$$

For the method to work properly, one HR-TEM image of a structure of interest L_2 and one HR-TEM image of unstrained known structure L_1, used to extract the distortions, should be taken at the same conditions. When L_2 is represented only in a part of the whole field of view of the image (for example, the case of a nanoparticle), the same area should represent L_1 in the second image. This will ensure that the distortions extracted from the second image match the ones present over the image of the L_2.

HR-STEM image - The displacement field components projected on the scan direction differ from one-pixel line to another by some varying translation values. Therefore, displacement fields are affected by scan distortions in all directions, unlike the projections of the reciprocal vectors. The scan distortions can be removed from a zone of interest provided some reference zone of known unstrained or constantly strained structure exists beneath or above the zone of interest in the 90° HR-STEM image. Only one 90° image is sufficient which is an essential advantage of such an approach.

We illustrate the method with a practical example. We consider a cross-sectional HR-STEM HAADF 90° image of (001) Si/a-SiO_x/(001) $SrTiO_3$/(001) $BaTiO_3$ structure, i.e. the scan direction is parallel to the vertical *z*-axis (Fig. 5(a)).

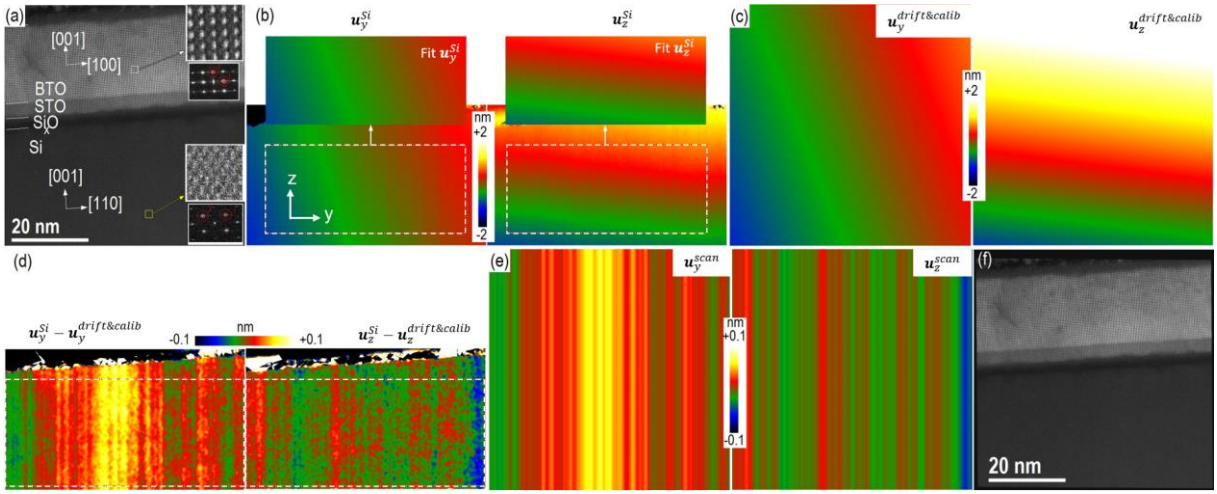

Fig. 5 Application of Abstrain-2nd to a single 90° HR-STEM image with a reference zone of known unstrained structure existing beneath the zone of interest: (a) HAADF HR-STEM image of (001) Si/a-SiO_x/(001) $SrTiO_3$/(001) $BaTiO_3$ structure; (b) displacement fields with reference to the Bravais lattice of Si structure. Inserts show the result of a linear fit applied to the internal zones marked by rectangular frames; (c) displacement fields, caused by a sample drift and pixel calibration error, extended over the whole field of view of (a); (d) displacement fields caused entirely by scan distortions in the reference zone. Rectangular frames indicate the zones used for averaging of the displacement fields in the vertical scan direction; (e) averaged displacement fields, caused by scan distortions, extended over the whole field of view of (a);(f) HR-STEM image corrected from all the distortions shown in (c) and (e).

In the bottom part of the image, the Si structure is seen along the $[1\bar{1}0]$ direction, with a 3 nm-thick amorphous SiO_x layer on top. In the upper part, a 4 nm-thick STO layer and a 20 nm-thick BTO layer on top are seen along the [010] direction. The image consists of 2048 x 2048 pixels presenting a 62 nm x 62 nm field of view. Each atomic column is represented by approximately 8 pixels (see inserts). The FFT patterns from the regions are inserted in the images. The red circles there indicate the reciprocal masks used for GPA with a radius corresponding to 0.8 nm spatial resolution in the real space.

First, we extract by using Eqs. (59-61) the displacement fields with reference to the Bravais lattice of Si structure in ***yz***-coordinate system, where ***y*** axis and ***z*** axis are horizontal and vertical, respectively (Fig. 5(b)). The displacement fields can be decomposed into linear and non-linear contributions. Scan distortions that induce displacement jumps in the direction perpendicular to the scan direction while remaining similar in the scan direction, define the non-linear part. Sample drift and pixel calibration error both induce linear displacement fields. The latter contribution can be obtained by applying a linear fit to ***y*** and ***z*** components of the displacement field extracted from the reference zone (see inserts in Fig. 5(b)). In practice, to avoid the impact of the image edges, such a procedure should be applied to some smaller internal zone of the reference one (see rectangular frames in Fig.5(b)). After partial derivation of such a linear displacement field (Eqs. (1-2)), we are left with the four constant values of strain tensor components and rigid body rotation induced by a sample drift and pixel calibration error distortions. The entire HR-STEM, not just the cut reference zone, is subjected to the same distortions. Thus, by substituting these constant values for ε_{ij}^0 and ω_{yz}^0 in Eqs. (60-61), we can generate, by using Eqs. (59), the corresponding displacement field, caused by a sample drift and pixel calibration error, over the whole field of view of the original HR-STEM image (Fig. 5(c)). The vertical bands of displacement jumps caused entirely by scan distortions are then recovered within the reference zone by subtracting the drift/calibration field from the original one (Fig. 5(d)). At the next stage, one should extend these bands over the whole field of view of the image. For this, we will use

the fact that scan distortions almost do not vary in the vertical, i.e. scan direction. Therefore, by averaging the displacement field induced by scan distortions in the vertical scan direction within the reference zone (see rectangular frames in Fig. 5(d)), the so-obtained one-pixel line profile can be repeated over the lines of the whole image, that provides the image of the displacement field solely caused by scan distortions (Fig. 5(e). When the latter is summed up with the previously determined drift/calibration displacement field (Fig. 5(c)), we get a displacement field related to all the distortions. Finally, such a displacement field should be subtracted from the one extracted within a zone of interest with reference to its corresponding Bravais lattice, that provides the correction of the latter. Alternatively, such a displacement field can be used to correct the original image itself (Fig. 5(a)) by using bi-linear interpolation. The resulting image corrected from all the distortions is presented in Fig. 5(f).

Table 1 outlines which of the methods, AbStrain-1st or AbStrain-2nd, is preferable to use for quantification of absolute strain tensor, rigid body rotation, interplanar distances, angles and displacement fields. Such a mapping is proposed over HR-TEM and HR-STEM images as a function of the relative position and shape of a structure of interest L_2 and known unstrained or constantly strained structure L_1, used for distortions correction.

Table 1 Scope of preferential application of AbStrain-1st or AbStrain-2nd to obtain absolute strain tensor, rigid body rotation, interplanar distances, angles and displacement fields over HR-TEM and HR-STEM images (L_2= structure of interest, L_1= known unstrained or constantly strained structure used for distortions correction)

Imaging/ Approach	Input images	Image conditions or requirements	Limits
HR-TEM AbStrain-2nd	Couple of images: one containing L_2 and one L_1 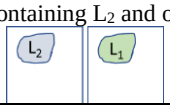	L_1 must occupy at least the same region as L_2	No limits
HR-STEM AbStrain-1st	Two couples of 0°/ 90° images: one containing L_2 and one L_1 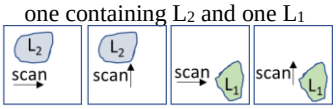	L_1 is not present over the field of view of L_2 image; L_1 and L_2 areas positions and shapes are independent	Displacement fields over rectangular entire crystalline regions by integration of strain tensor and rigid body rotation maps; Displacement fields will contain errors induced by inevitable misalignment of atomic positions in 0° and 90° images subjected to different distortions
	Couple of 0° and 90° images both containing L_2 and L_1 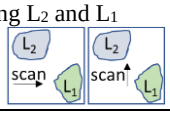	L_1 and L_2 are both present over the field of view of the image with no constraint about their relative positions	
HR-STEM AbStrain-2nd	One 90° image containing both L_2 and L_1 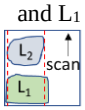	L_1 and L_2 are both present over the field of view of the image; L_1 must be beneath or above L_2 with a horizontal size ≥ that of L_2 (see dotted red lines)	No limits
	Two couples of 0°/90° images: one containing L_2 and one L_1 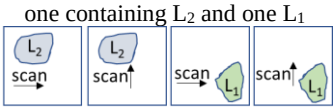	L_1 is not present over the field of view of L_2 image; Preliminary Ophus treatment of 0°/ 90° images of L_2 and L_1 in order to get rid of scan distortions	High-enough contrast and large-enough number of pixels per atomic column are required to ensure feasibility of Ophus treatment, that limits the size of attainable field of view

As follows from the first row of Table 1, HR-TEM images are to be preferably treated by AbStrain-2nd, provided that L_1 and L_2 structures occupy the same region over the corresponding field of view.

Crystals of arbitrary configurations can be analyzed, including, for example, nanoparticles embedded within amorphous matrix.

When to HR-STEM images, the choice of the approach depends on the real situation.

When L_1 is not present with L_2 in the field of view of the image (second row in Table 1), the correction of scan distortions becomes possible only with AbStrain-1st. Here, one needs to acquire two couples of 0° and 90° images, one of which contains L_2 and the other one L_1 structures. While strain tensor and rigid body rotation can be extracted for arbitrary structure configurations, displacement fields can be obtained provided that crystalline regions of structures are not interrupted by amorphous inserts along the orthogonal paths of strain field integration. Moreover, since 0° and 90° images are differently distorted, the images are inevitably misaligned. This will introduce errors during integration. Alternatively, for general structural configurations of L_1 and L_2, the couples of 0° and 90° images can be subjected to Ophus treatment [30] which allows to suppress the effect of scan distortions over the resulting image. Then, AbStrain-2nd can be applied (last row in Table 1).

When L_1 is present over the field of view of L_2 image (third row in Table 1), but L_1 is not necessarily beneath or above L_2, AbStrain-1stcan be applied for a single couple of 0° and 90° images with the previously described limitation on getting the displacement field. Otherwise, when L_1 and L_2 are both present over the field of view of the image, L_1 is located beneath or above L_2, and the horizontal size of L_1 is not less than that of L_2, a single 90° image is sufficient for the application of AbStrain-2nd for an arbitrary L_2 structure configuration (fourth row in Table 1).

3. RELATIVE DISPLACEMENT FIELD

For practical applications of AbStrain to materials composed of different atoms, each having its own sub-structure, one can be interested in the analysis of strain and displacements within each sub-structure independently of the others with reference to a Bravais lattice or, alternatively, with reference to each other. First, we propose here the method for the construction of images of each sub-structure contained in an original image. Then, the aforementioned AbStrain techniques can be used to treat such images individually.

Regarding relative displacements of sub-structures, we describe the procedure for quantifying their continuous or discrete values without the need to take into account image distortions and the structural characteristics of the crystal, such as the {h,k,l} indices and lattice parameters. We refer to the method as "Relative displacement".

3.1 Decomposition of HR-(S)TEM image into images of sub-structures

For simplicity, let us consider the case of two sub-structures, sub-structure A and sub-structure B. By filtering the original image, it is possible to isolate the lattice fringes associated with sub-structures A and B that might have similar or different peak intensities. Our proposal is to construct and apply an appropriate mask.

Figure 6(a) shows a cross-sectional (1-10) HAADF HR-STEM image of $SrTiO_3$ where sub-structures A and B are composed of Sr and Ti atoms, respectively. The isolation of the sub-structure A fringes is done in two steps. We begin by constructing a first mask by applying GPA to the ZOI of the

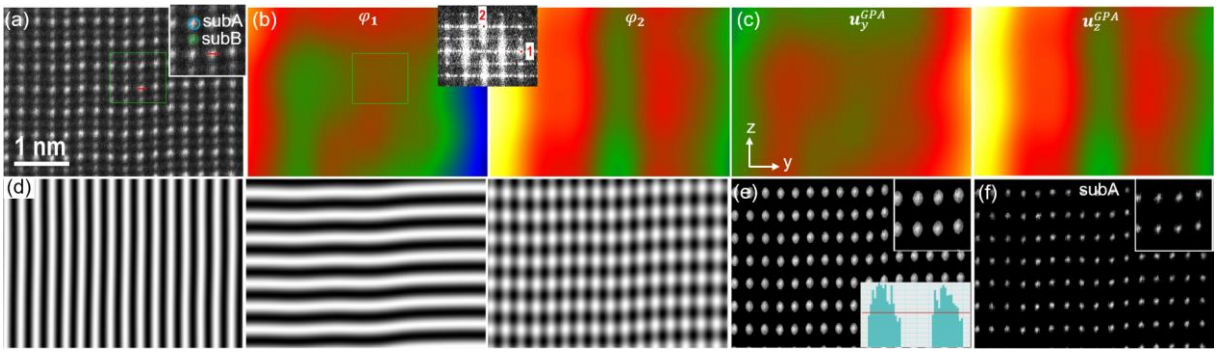

Fig. 6 Decomposition of an HR-STEM image into images of sub-structures (isolation of sub-structure A is illustrated here): (a) cross-sectional (1-10) HAADF HR-STEM image of $SrTiO_3$. Insert shows the atoms of sub-structure A (Sr) and B (Ti). The red trace centered over the Sr atom within the reference zone of GPA provides(i_0^{col}, i_0^{row}) for substitution in Eq.64 ; (b) geometric phases obtained by GPA; (c) displacement fields obtained by GPA; (d) $Mask_n$ corresponding to $\boldsymbol{g}_1 = 220$, $P_1 = 2$ and $\boldsymbol{g}_2 = 002$, $P_2 = 2$ and their sum; (e) image obtained by application of the mask sum in (d). Insert shows the intensity profile over two Sr atoms. Red line indicates a threshold value used to replace all the intensities of a lower magnitude in the image; (f) image of selected sub-structure A with the background equal to the threshold value.

image, then selecting two appropriate reciprocal vectors $\boldsymbol{g}_1$ and $\boldsymbol{g}_2$ in FFT (see insert in Fig. 6(b)), extracting the corresponding geometric phases, φ_1 and φ_2 (Fig. 6(b)) and the displacement components, $\boldsymbol{u}_y^{GPA}$ and $\boldsymbol{u}_z^{GPA}$(Fig. 6(c)). The latter are used to create a mask (Fig. 6(d)) which consists of two sets of cosines like fringes as

$$Mask_n = \frac{1}{2}\cos\left(\frac{2\pi}{P_n}\left(\left(i_0^{col} - i^{col} + \frac{\boldsymbol{u}_y^{GPA}}{px}\right)\mathrm{g}_{ny}^0 + \left(i^{row} - i_0^{row} + \frac{\boldsymbol{u}_z^{GPA}}{px}\right)\mathrm{g}_{nz}^0\right)\right),$$
$$Mask = \sum_{n=1}^{2} Mask_n \qquad (64)$$

where the integers P_n $(\mathrm{n} = 1 \text{ and } 2)$ define the periods of the mask fringes and $\left(i_0^{col}, i_0^{row}\right)$ are user-defined coordinates of one of the atoms of the sub-structure A within the GPA reference zone (see the trace in insert of Fig. 6(a) centered over the A atom). In the example shown in Fig. 6(a), we intend to extract (110) and (001) planes of sub-structure A. To suppress the effect of B atoms on the displacement fields extracted for sub-structure A, we have used $\boldsymbol{g}_1 = 220$, $P_1 = 2$ and $\boldsymbol{g}_2 = 002$, $P_2 = 2$.

Once created, the aperture of the passing array of the mask is adjusted by filtering all intensities less than some user-chosen threshold value within the range from 0 to 1 and then applied to the original image (Fig. 6(e)). After thresholding the obtained image to preserve the contrast symmetry of the atomic columns (insert in Fig. 6(e), the image of sub-structure A is obtained (Fig. 6(f)). Since intensities are solely emanating from the fringes of sub-structure A, this new image can be used, if necessary, to repeat the mask construction process with $\boldsymbol{g}_1 = 110, P_1 = 1$ and $\boldsymbol{g}_2 = 001, P_2 = 1$, and apply it to the original image. This will ensure the absence of any impact of sub-structure B on $\boldsymbol{u}^{GPA}$ and, thus, a more correct positioning of the mask relative to sub-structure A in the original image.

To isolate the fringes of sub-structure B, we subtract the image in Fig. 6(e) from the original one and extract $\boldsymbol{u}^{GPA}$. By doing so, the contribution of the fringes of sub-structure A to $\boldsymbol{u}^{GPA}$ will be somehow vanished. Afterwards, as for sub-structure A, the mask creation process should be repeated twice (for refining purposes) and applied to the original image. The image of sub-structure B is obtained.

3.2 Relative displacement of sub-structure B with reference to sub-structure A

When the structure is composed of 2 sub-structures A and B or more, one can be interested in the relative displacement of atoms of sub-structure B with respect to sub-structure A, for example, sub-structure B with respect to the barycenter of the cells constituting sub-structure A (Fig. 1(d)).

For this, after the reconstruction of the images of each sub-structure from the original HR-STEM image (see section 3.1), the relative displacement between the barycenter of the cells of sub-structure A and the atoms of sub-structure B can be defined as

$$\Delta \boldsymbol{u}_y^{SL_{subB-A}}(\boldsymbol{r}) = \boldsymbol{u}_y^{SL_{subB}}(\boldsymbol{r}) - \boldsymbol{u}_y^{SL_{subA}}(\boldsymbol{r}) + \Delta \boldsymbol{u}_y^{0_{subB-A}}(\boldsymbol{r_0}), \quad (65)$$

$$\Delta \boldsymbol{u}_z^{SL_{subB-A}}(\boldsymbol{r}) = \boldsymbol{u}_z^{SL_{subB}}(\boldsymbol{r}) - \boldsymbol{u}_z^{SL_{subA}}(\boldsymbol{r}) + \Delta \boldsymbol{u}_z^{0_{subB-A}}(\boldsymbol{r_0}), \quad (66)$$

where $\Delta \boldsymbol{u}_y^{0_{subB-A}}(\boldsymbol{r_0})$ and $\Delta \boldsymbol{u}_z^{0_{subB-A}}(\boldsymbol{r_0})$ are the constant values corresponding to the components of the displacement field of sub-structure B with reference to the position of barycenter of the cells composed of atoms of sub-structure A which are located in the reference zone (Fig. 1(d)). Because usually the distance between the barycenter of sub-structure A and atoms of sub-structure B is small when compared to a distance between neighboring atoms of any of sub-structures, one can neglect a difference in distortions accumulating at such a distance. Therefore, the distortions are omitted in Eqs. (65-66).

The boundary conditions of Eqs. (65-66) impose that $\Delta \boldsymbol{u}^{SL_{subB-A}}(\boldsymbol{r_0}) = \Delta \boldsymbol{u}^{0_{subB-A}}(\boldsymbol{r_0})$ and $\boldsymbol{u}^{SL_{subB}}(\boldsymbol{r_0}) = \boldsymbol{u}^{SL_{subA}}(\boldsymbol{r_0}) = 0$. Due to the difference in contrast and positions of atoms of the sub-structures, neither of these conditions can be satisfied by a direct application of GPA to two different images of sub-structures A and B, even with reference to the same zone in the corresponding images. Due to the intrinsic working mode of GPA, if $\boldsymbol{u}^{SL_{subA}}$ equals zero at $\boldsymbol{r}_0$, $\boldsymbol{u}^{SL_{subB}}$ maybe not, it will be equal to zero at some other position within the reference zone. Secondly, neither of the displacement fields contains information on $\Delta u_y^{0_{subB-A}}(\boldsymbol{r_0})$.

In order that displacement fields extracted by GPA satisfy the required boundary and infinitesimal strain approximation conditions, a reference structure should be the same for both images with a periodicity similar to that of the experimental image of sub-structure A. A reference structure which meets such a requirement should be composed of Gaussian-like spots repeating the contrast, the periodicity and the positions of atoms of sub-structure A in some reference zone of the corresponding image (further on referred to as "refA"). Such a structure can be simulated in form of an image further on referred to as "A_{sim}". For sub-structure B, the simulated image B_{sim} should preserve exactly the periodicity of A_{sim}, have a contrast similar to that of sub-structure B and the Gaussian-like spots have to be shifted, with respect to A_{sim}, by the barycenter vector of the A cells it is composed of (Fig. 1(d)). Further on, A_{sim} and B_{sim} must be used as the reference zones for GPA of the images composed of experimental and simulated parts. The image with sub-structure B will provide the displacement of B atoms with respect to the fixed position of the barycenter of A in ref A, $\boldsymbol{u}^{SL_{subB-refA}}(\boldsymbol{r})$. The image with sub-structure A will provide the displacement of A atoms with respect to the positions of A atoms constructing the barycenter of A in ref A, $\boldsymbol{u}^{SL_{subA-refA}}(\boldsymbol{r})$. Finally, the difference between the displacement fields obtained over experimental parts of the images of sub-structure B and that of sub-structure A will correspond to the definition used in Eqs. (65-66).

In order to calculate the coordinates of the barycenter of a cell composed of A atoms in refA, one should first calculate the coordinates of atoms from which it is composed of (Fig. 1(d), blue open circles). For this, we will use the inverse transformation of the reciprocal space cell composed of $\boldsymbol{g}_1^0$ and $\boldsymbol{g}_2^0$ vectors measured by GPA in refA. The coordinates of the so calculated $\boldsymbol{a}_1^0$ and $\boldsymbol{a}_2^0$ are given by

$$a_{1y}^0 = px\frac{g_{2z}^O}{\left|g_{1z}^O g_{2y}^O - g_{1y}^O g_{2z}^O\right|}, a_{1z}^0 = -px\frac{g_{2y}^O}{\left|g_{1z}^O g_{2y}^O - g_{1y}^O g_{2z}^O\right|},$$
$$a_{2y}^0 = -px\frac{g_{1z}^O}{\left|g_{1z}^O g_{2y}^O - g_{1y}^O g_{2z}^O\right|}, a_{2z}^0 = px\frac{g_{1y}^O}{\left|g_{1z}^O g_{2y}^O - g_{1y}^O g_{2z}^O\right|}. \quad (67)$$

The barycenter vector is given then by

$$\boldsymbol{a}_c^0 = k_1\boldsymbol{a}_1^0 + k_2\boldsymbol{a}_2^0, \quad (68)$$

where k_1 and k_2 are the coefficients which can be chosen as a function of the real structure. The $\boldsymbol{a}_c^0$ vector depicted in Fig. 1(d) corresponds to $k_1 = k_2 = 0.5$, i.e. barycenter is chosen at the intersection of the diagonals of the $(\boldsymbol{a}_1^0, \boldsymbol{a}_2^0)$ cell.

Two images, A_{sim} and B_{sim}, are simulated from the repeating $(\boldsymbol{a}_1^0, \boldsymbol{a}_2^0)$ cell. Such images can be created in the form of

$$A_{sim} = \mathrm{I}^{pic_A}\left(1 - \frac{4 - Mask_A}{4\,\mathrm{f}^{pic_A}\,\mathrm{N}}\right), \quad (69)$$

$$B_{sim} = \mathrm{I}^{pic_B}\left(1 - \frac{4 - Mask_B}{4\,\mathrm{f}^{pic_B}\,\mathrm{N}}\right), \quad (70)$$

where I^{pic_A} with I^{pic_B} and f^{pic_A} with f^{pic_B} are characteristic values of peak intensity and full-width-at-half-maximum of the atoms of sub-structures A and B in refA, N is the largest value between the norms $\left\|\boldsymbol{g}_1^O\right\|$ and $\left\|\boldsymbol{g}_2^O\right\|$ and

$$Mask_A = \sum_{n=1}^{2}\cos\left(2\pi\left((i_0^{col} - i^{col})\mathrm{g}_{ny}^0 + (i^{row} - i_0^{row})\mathrm{g}_{nz}^0\right)\right), \quad (71)$$

$$Mask_B = \sum_{n=1}^{2}\cos\left(2\pi\left(k_n + (i_0^{col} - i^{col})\mathrm{g}_{ny}^0 + (i^{row} - i_0^{row})\mathrm{g}_{nz}^0\right)\right). \quad (72)$$

where $\left(i_0^{col}, i_0^{row}\right)$ are user-defined coordinates of one of the atoms of sub-structure A within refA. A_{sim} and B_{sim} are set to zero when Eqs. (69-70) provide negative values. As a result, the peak positions and contrast of the simulated atoms in the A_{sim} closely resemble those of the experimental ones in refA. The B_{sim} formed by shifting the A_{sim} by $\boldsymbol{a}_c^0$ (Fig. 1(d)) preserves its periodicity and obeys the contrast similar to that of sub-structure B.

A_{sim} and B_{sim} are given the same width as the experimental ones and extended below the experimental images, getting the doubled height. Afterwards, the simulated images A_{sim} and B_{sim} should be combined with the corresponding experimental ones in order to be used as the reference zones for GPA. As an example, we will use the images of the sub-structures A (Sr and Ba atoms) and B (Ti atoms) obtained by the decomposition of the image shown in Fig. 5(a). These images are used to construct A_{sim} and B_{sim} with the contrast and positions of simulated atoms corresponding to that of sub-structure A and B in refA. We constructed a couple of images A_{sim}&A and B_{sim}&B (Fig. 7(a) and (b)). The upper and the lower halves of A_{sim}&A and B_{sim}&B are defined by the experimental and simulated images of the sub-structures A and B, respectively.

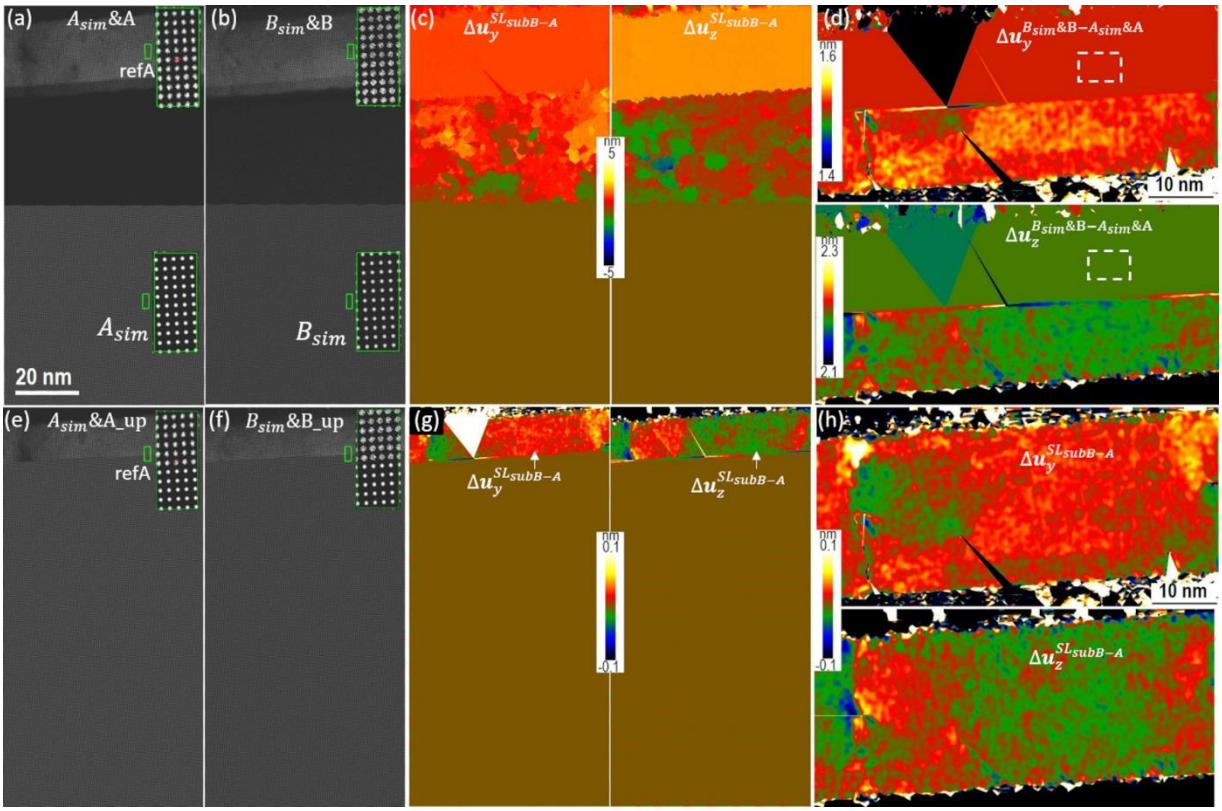

Fig. 7 (a) and (b) Images constructed from sub-structure A and B obtained by the decomposition of HR-STEM HAADF image in Fig. 5a and the corresponding simulated images A_{sim} and B_{sim}. refA indicates the reference zone used by GPA. Red line indicates the trace centered over the A atom within refA providing (i_0^{col}, i_0^{row}); (c) relative displacement fields $\Delta\boldsymbol{u}^{SL_{subB-A}}$ obtained with reference to the simulated structures in (a) and (b);(e) and (f) Images constructed from sub-structure A and B above refA obtained by the decomposition of HR-STEM HAADF image in Fig. 5a and the corresponding simulated images A_{sim} and B_{sim}; (g) relative displacement fields $\Delta\boldsymbol{u}^{SL_{subB-A}}$ obtained with reference to the simulated structures in (e) and (f);(d) displacement fields errors $\Delta\boldsymbol{u}^{B_{sim}\&B-A_{sim}\&A}$ obtained by subtraction of (g) from (c); (h) relative displacement fields $\Delta\boldsymbol{u}^{SL_{subB-A}}$ corrected from the displacement fields errors $\Delta\boldsymbol{u}^{B_{sim}\&B-A_{sim}\&A}$ measured above refA within white rectangles shown in (d).

At first sight, the use of the bottom parts of these images like a reference zone for GPA and subtraction of the displacement fields extracted over A_{sim}&A from that obtained over B_{sim}&B will provide the required solution for Eqs. (65-66) (Fig. 7(c)). However, the positions and contrast of atoms in A and B might differ a lot at the interface between simulated and experimental parts of the images and infinitesimal strain approximation becomes not valid there. If it is the case, the displacement field extracted by GPA within sub-structure A and B will be affected by two different and arbitrary constant displacement jumps values $\Delta\boldsymbol{u}^{A_{sim}\&A}$ and $\Delta\boldsymbol{u}^{B_{sim}\&B}$

$$\boldsymbol{u}^{A_{sim}\&A}(\boldsymbol{r}) = \boldsymbol{u}^{SL_{subA-refA}}(\boldsymbol{r}) + \Delta\boldsymbol{u}^{A_{sim}\&A}, \tag{73}$$

$$\boldsymbol{u}^{B_{sim}\&B}(\boldsymbol{r}) = \boldsymbol{u}^{SL_{subB-refA}}(\boldsymbol{r}) + \Delta\boldsymbol{u}^{B_{sim}\&B} \tag{74}$$

The resulting relative displacement fields, $\Delta\boldsymbol{u}^{SL_{subB-A}}$ (Fig. 7(c))

$$\Delta\boldsymbol{u}^{SL_{subB-A}} = \boldsymbol{u}^{SL_{subB-refA}}(\boldsymbol{r}) - \boldsymbol{u}^{SL_{subB-refA}}(\boldsymbol{r}) + \Delta\boldsymbol{u}^{B_{sim}\&B-A_{sim}\&A}, \tag{75}$$

will contain the required relative displacement fields, $\boldsymbol{u}^{SL_{subB-refA}}(\boldsymbol{r}) - \boldsymbol{u}^{SL_{subB-refA}}(\boldsymbol{r})$ and constant arbitrary error values $\Delta\boldsymbol{u}^{B_{sim}\&B-A_{sim}\&A} = \Delta\boldsymbol{u}^{B_{sim}\&B} - \Delta\boldsymbol{u}^{A_{sim}\&A}$ which should be removed over the whole field of view.

To overcome such a problem, we extract these error values from the area in a close vicinity of refA. For this, we construct a couple of images $A_{sim}\&\mathrm{A}_{up}$ and $B_{sim}\&\mathrm{B}_{up}$ where the parts of A_{sim} and B_{sim} located just above refA are replaced by the corresponding parts of the experimental images, with an interface along $\boldsymbol{a}_1^0$ (Fig. 7(e) and (f)). By doing so, we ensure the validity of the infinitesimal strain approximation at least in a close vicinity of refA where the contrast and the positions of simulated and experimental atoms are very similar. Although they are not exactly identical, some small and exactly the same constant displacement jumps $\Delta\boldsymbol{u}$ will arise at the interface between the simulated and experimental parts of $A_{sim}\&\mathrm{A}_{up}$ and $B_{sim}\&\mathrm{B}_{up}$

$$\boldsymbol{u}^{A_{sim}\&\mathrm{A}_{up}}(\boldsymbol{r}) = \boldsymbol{u}^{SL_{subA-refA}}(\boldsymbol{r}) + \Delta\boldsymbol{u}\,, \tag{76}$$

$$\boldsymbol{u}^{B_{sim}\&\mathrm{B}_{up}}(\boldsymbol{r}) = \boldsymbol{u}^{SL_{subB-refA}}(\boldsymbol{r}) + \Delta\boldsymbol{u}, \tag{77}$$

The difference between these displacement fields will give us immediately the required relative displacement in this upper part of the whole field of view (Fig. 7(g))

$$\Delta\boldsymbol{u}^{SL_{subB-A}} = \boldsymbol{u}^{SL_{subB-refA}}(\boldsymbol{r}) - \boldsymbol{u}^{SL_{subB-refA}}(\boldsymbol{r}). \tag{78}$$

By comparing Eqs. (75) and (78), it becomes evident that the constant error values of $\Delta\boldsymbol{u}^{B_{sim}\&\mathrm{B}-A_{sim}\&\mathrm{A}}$ can be extracted from the zone above refA of $A_{sim}\&\mathrm{A}$ and $B_{sim}\&\mathrm{B}$ (Fig.7(d), white rectangles). For this, the image of $\Delta\boldsymbol{u}^{SL_{subB-A}}(\boldsymbol{r})$ corresponding to $A_{sim}\&\mathrm{A}_{up}$ and $B_{sim}\&\mathrm{B}_{up}$ should be subtracted from that corresponding to $A_{sim}\&\mathrm{A}$ and $B_{sim}\&\mathrm{B}$. The eventual relative displacement field corrected from the errors is obtained by subtracting these values from the whole field of view of $\Delta\boldsymbol{u}^{SL_{subB-A}}(\boldsymbol{r})$ corresponding to $A_{sim}\&\mathrm{A}$ and $B_{sim}\&\mathrm{B}$ (Fig. 7(h)).

As follows from such a description, relative displacement of sub-structures can be extracted over a single HR-STEM image of a general structure without the need to account for image distortions and be familiar with the crystal's structural characteristics.

In the following, we present the application of AbStrain to map absolute displacements, strain tensor, rigid body rotation, interplanar distances and angles with reference to a Bravais lattice, as well as the application of Relative displacement to map relative displacement fields of sub-structures, over cross-sectional HAADF HR-STEM images of (001) Si/a-SiO_x/(001) $SrTiO_3$/(001) $BaTiO_3$ structure shown in Fig. 5a.

4. APPLICATION OF ABSTRAIN AND RELATIVE DISPLACEMENT TO HR-STEM IMAGES

Figure 8(a-i) shows the absolute displacement fields, interplanar distances and angles, strain tensor components and rigid body rotation, with reference to the Bravais lattice of BTO (tetragonal, space group P4mm, $a^{\mathrm{BTO}} = 0.3991$ nm, c^{BTO} = 0.4035 nm), obtained by AbStrain-2nd (forth row in Table 1) for sub-structure A (Sr+Ba atoms) which was isolated from the single 90° image shown in Fig. 5(a). The maps are obtained in the $\boldsymbol{y}'\boldsymbol{z}'$-coordinate system where $\boldsymbol{y}' = [100]^{BTO}$ and $\boldsymbol{z}' = [001]^{BTO}$. The values were corrected from all the distortions (section 2.6) using the displacement fields measured in the Si structure imaged beneath (Fig.5(c) and (e)).

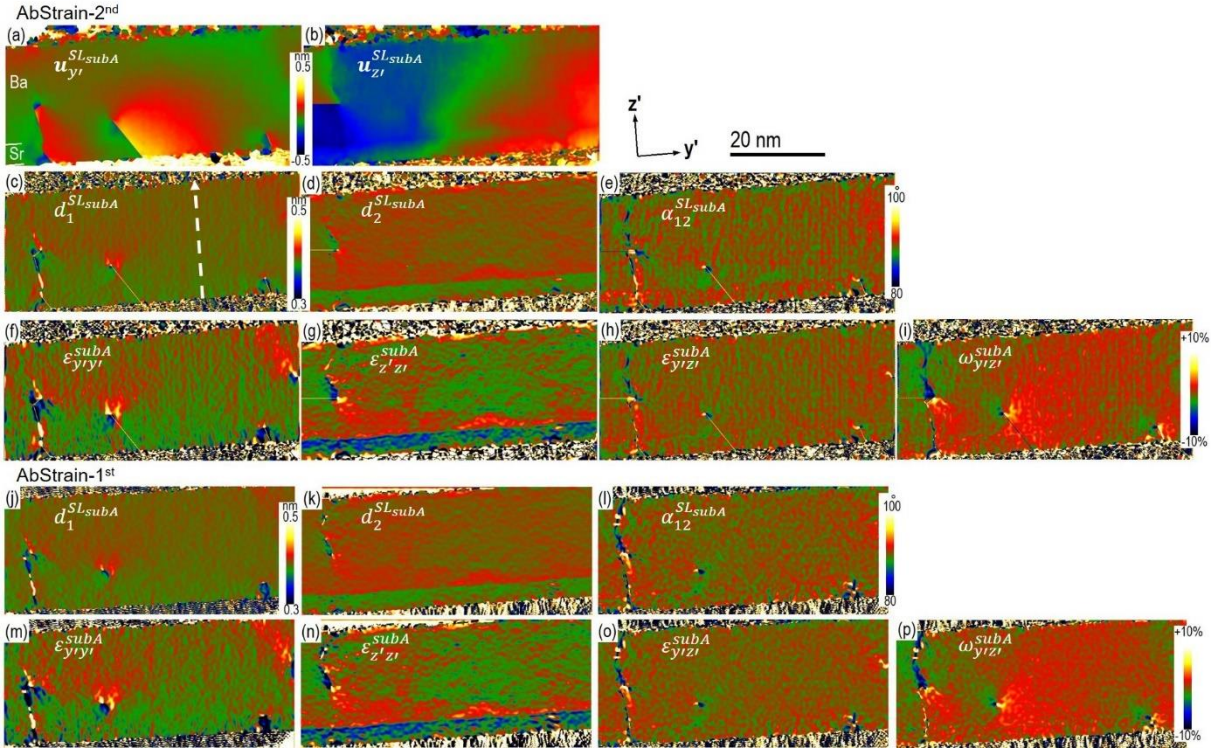

Fig. 8 (a-i) AbStrain-2nd approach applied to sub-structure A of the 90° image of Fig.5(a): displacement fields (a,b), interplanar distances and angle (c-e), strain tensor and rigid body rotation (f-i) corrected from the distortions by using Si structure imaged beneath; (j-p) AbStrain-1st approach applied to sub-structure A of the 0° image (not shown) and 90° image of Fig. 5(a): interplanar distances and angle (j-l), strain tensor and rigid body rotation (m-p) corrected from the distortions by using separate 0° and 90° images of Si structure of Fig.4(a). The data are obtained with reference to the Bravais lattice of BTO in the $\boldsymbol{y'z'}$*-coordinate system.*

A number of dislocations are present in the BTO layer, as evidenced by the jumps in the displacement fields (Fig. 8(a), (b)). When we consider the dislocation seen in the middle of the images, the jumps of ***y'***-component and ***z'***-component of the displacement field are measured to be of 0.3997 nm and 0 nm, respectively, which indicates that this is a misfit edge-type dislocation with the in-plane Burgers vector equal $\boldsymbol{b} = a^{\mathrm{BTO}}[100]$.

The strain tensor and rigid body rotation maps (Fig. 8(f-i)) were extracted after partial derivation of the displacement fields. Some residual tiny vertical lines are left in Fig. 8(f), (h) and (i) which indicates a not perfect correction of the scan distortions. The presence of dislocations and/or too different interplanar distances in a ZOI in comparison to the Si part of the image used for correction may cause such an effect. In fact, the same shift of the intensities over the atomic columns caused by the probe scan unintended positioning might result in slightly different displacement error over these different zones of the image. Anyway, these residual distortions have an amplitude similar to the average noise-to-signal ratio and thus, have a negligible impact on the accuracy of so obtained values.

In the right half of the strain tensor maps we note almost zero shear strain, anticlockwise rigid body rotation, a continuously changing in-plane compressive strain and a specific distribution of tensile (red) then compressive (green) out-of-plane strain within the BTO layer going from the substrate to the surface of the film along ***z'***. The tensile strain has a triangular like distribution within first 3 nm-thick layer which then changes quite abruptly its sign to negative values i.e. strain becomes compressive.

For comparison with the most general case (second row in Table 1), we applied AbStrain-1st using a couple of 0° and 90° images of sub-structure A and a couple of 0° and 90° images of Si shown in Fig. 4(a). The values in sub-structure A were corrected from all the distortions (section 2.3) by subtraction of the strain fields measured in the separate images of Si (Fig.4(d)). Figure 8(j-p) shows the resulting maps of interplanar distances and angles, strain tensor components and rigid body rotation, with the same reference to Bravais lattice of BTO and for the same coordinate system as shown in Fig. 8(a-i). Due to the misalignment of 0° and 90° images, the common field of view is slightly reduced in comparison to the original size of the images.

The results look very similar to that obtained by AbStrain-2nd with no signature of residual scan distortions. In order to get a quantitative comparison, we first plot the depth profiles of the strain tensor and rigid body rotation (Fig. 9(a)) extracted from Fig. 8 (f-i) and (m-p) along the position of the dashed arrow depicted in Fig. 8(c) and averaged over 20 nm along the in-plane direction. Both methods provide very similar results.

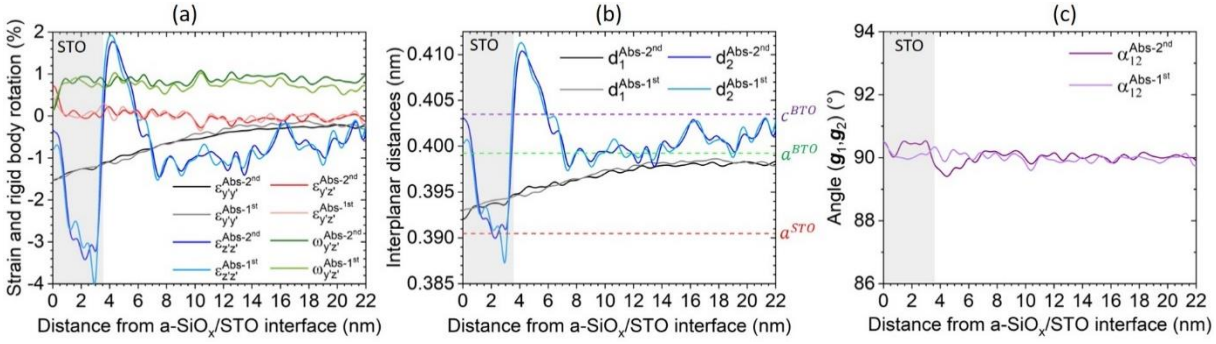

Fig. 9 Depth profiles of: (a) strain tensor and rigid body rotation from Fig. 8 (f-i) and (m-p); (b) interplanar distances from Fig. 8 (c, d) and (j, k); (c) angle between $\boldsymbol{g}_1^{STO/BTO}$ and $\boldsymbol{g}_2^{STO/BTO}$ from Fig. 8(e) and (l), obtained for sub-structure A by AbStrain-1st and AbStrain-2nd. The profiles are obtained along the position of the dashed arrow depicted in Fig. 8 (c) and averaged over 20 nm along the in-plane direction. The position of the STO layer is marked by grey band.

The positive rigid body rotation value measured in that zone reflects the impact of the dislocations presenting in the BTO layer (Fig. 8(i), (p)). It is interesting to note that the in-plane strain is always negative and continuously decreases in amplitude from -1.2 % to -0.2% at the BTO layer surface, when measured from the STO/BTO interface. The compressive strain is expected owing to the lattice parameter differences between the perovskite structure of STO or BTO and the Si one. The progressive decrease of the strain is consistent with a partial in-plane stress relaxation in the BTO layer due to formation of misfit dislocations. Because no any force acts on the free surface of the BTO layer in the z' direction, one would expect a tensile out-of-plane strain all over the BTO layer, consistent with the Poisson reaction. While it holds true within the first 3 nm when measured from the STO/BTO interface, compressive out-of-plane strain above must indicate that the BTO layer has been subjected to in-plane tensile stress there, which is not the case. As a hypothesis one can suppose a change in the alignment of the c-axis of the BTO cell along the direction of observation, which would require a change of the orientation of the reference Bravais cell in AbStrain calculation. In such a case, instead of projection of the BTO crystal along the [010] direction in the image plane, we deal with the [001] projection above the first 3 nm of the BTO layer. To be consistent with the strain values measured there, the BTO structure should be almost fully plastically relaxed in the [001] direction parallel to the [100] direction in STO. Such a hypothesis is quite consistent with the evolution of the BTO interplanar distances presented in Fig. 9(b). While the in-plane interplanar distance is always lower than a^{BTO}**,** i.e. the BTO structure is always compressed in the in-plane direction, the out-of-plane interplanar distance is larger

than c^{BTO} only within the first 3 nm distance from the STO/BTO interface. Above it remains equal or slightly larger than a^{BTO}. As for strain, both AbStrain-2nd and AbStrain-1st provide very similar quantitative values. Regarding the angle between $\boldsymbol{g}_1^{STO/BTO}$ and $\boldsymbol{g}_2^{STO/BTO}$, which depth evolution is presented in Fig. 9(c), it slightly differs from a 90° value within the first 6 nm distance from the STO bottom interface before it stabilizes to a value of 90° within BTO. Overall, such a complex strain and displacement distributions within the BTO layer require 3D modelling of the structure and of its behavior under applied stress [6,7, 25-27], which is out of the scope of the present paper.

Figure 10(a) shows the map of the amplitude and Figure 10(b) of the angle between the displacement vector and ***y'***-axis of the relative displacement between the sub-structure of Ti atoms and the sub-structure of barycenters of the cells composed of Sr+Ba atoms recalculated by Relative displacement from that obtained in ***yz***-coordinate system (see section 3.2, Fig. 7(h)). It is another way to represent the corresponding displacement fields in continuous form.

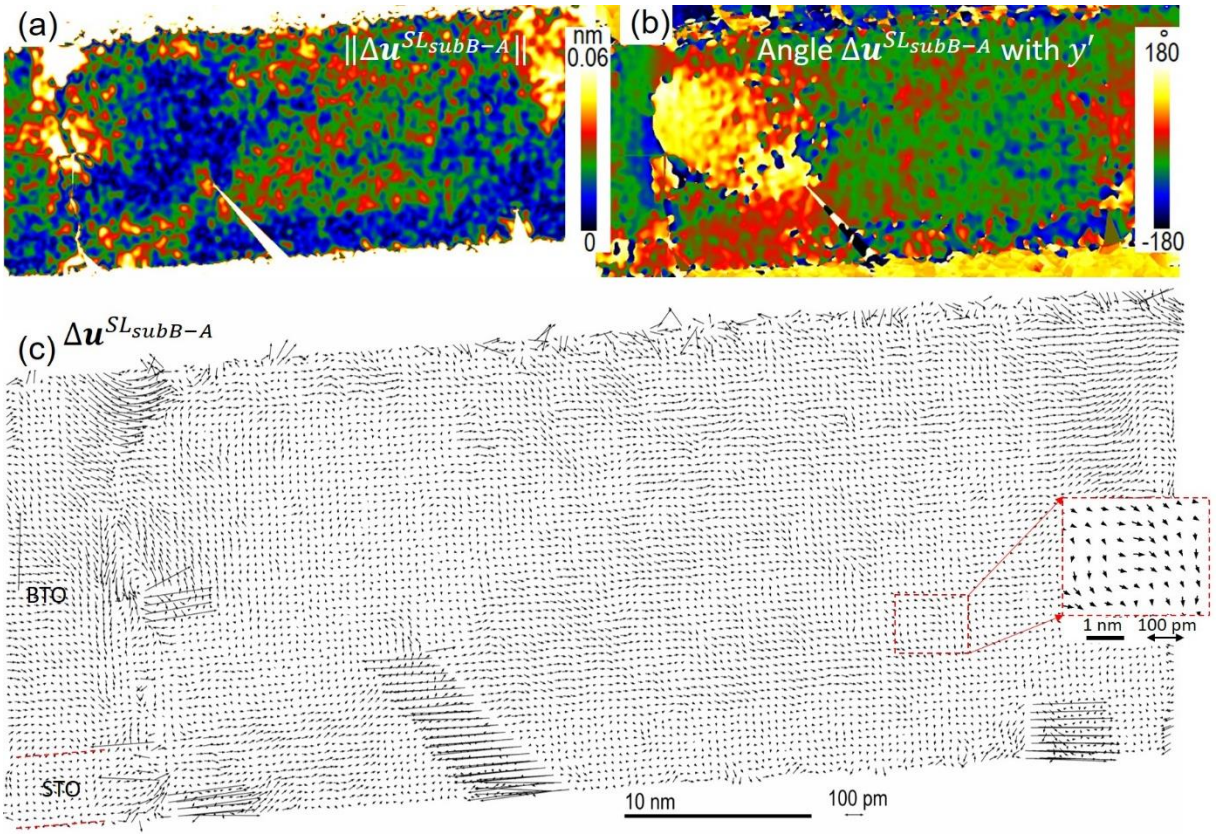

*Fig. 10 Relative displacement between the sub-structure of Ti atoms and the sub-structure of barycenters of the cells composed of Sr+Ba atoms presented in continuous (a, b) and discrete (c) forms: (a) displacement's amplitude; (b) angle between the displacement's direction and **y'**-axis. Insert in (c) shows the zoomed part of the characteristic pattern of the relative displacement in BTO.*

One can clearly see that the amplitude of the relative displacement is almost zero in the STO layer and in some parts of the BTO layer related to the positions of dislocations cores. In other regions, the relative displacement changes its direction and amplitude reaching a value of 40 pm.

Another possible representation for displacement fields in the form of arrows is shown in Figure 10 (c). Here, the length of an arrow denotes the displacement's amplitude measured at the location of the barycenter of Sr+Ba sub-structure (see the scale bar in the form of a double arrow), and its direction denotes the direction of the displacement. Unlike the continuous displacement fields shown in Fig. 10 (a-b), this map of discrete values is a typical representation of the relative displacement field provided

by “peak finding” methods [19-22]. In the regions of the dislocations, few 100 pm long arrows are presented. These arrows represent a discontinuity of the displacement field around the dislocation cores, where we get a jump in displacement, with reference to A_{sim} lattice (see section 3.2), equal the sum of the relative displacement $\Delta \boldsymbol{u}^{SL_{subB-A}}$ and the projection of the Burgers vector in the image plane. It is evident that the rest of the BTO layer contains several nanometer-large blocks with different relative displacement orientations (see insert). The displacement’s amplitude varies from 5 to 40 pm. It would be necessary to model such a structure in order to analyze this behavior in greater depth, which is outside the scope of the current paper.

5. CONCLUSIONS

In this work, we overcome the limitation of using *similar* reference crystal structure over the same field of view for the reciprocal space treatment of HR-TEM and HR-STEM images like with GPA, by directly treating the zone of interest. We propose to reconstruct the displacement fields and strain tensor components of the imaged structure with reference to a user-defined Bravais lattice. We provided the corresponding mathematical formalism and developed the method, named Absolute Strain (AbStrain), with two approaches. The first one provides the components of an absolute strain tensor and rigid body rotation by using the maps of measured reciprocal space vectors and the coordinates of reciprocal space vectors of the virtual unstrained structure. Displacement field is then calculated by integration of such a strain tensor and rigid body rotation over a specific path, which we presented. Alternatively, the second approach allows for the reconstruction of an absolute displacement field with reference to a Bravais lattice, from which an absolute strain tensor and rigid body rotation are obtained by partial derivation. Interplanar distances and angles are reconstructed within both approaches from the absolute strain tensor and rigid body rotation maps.

Since absolute values of atomic positions over the experimental images are affected by different types of image distortions, we also presented the main procedures for their correction, specific to HR-TEM and HR-STEM imaging. Regarding HR-TEM images, the distortions induced by the projected lens, CCD camera and pixel calibration errors are corrected by using some other image of known and arbitrary structure taken at the same conditions. Regarding HR-STEM images, the methods allow to correct for scan, sample drift and pixel calibration error distortions. When strain tensor is the only concern, Abstrain-1st can be successfully applied to a couple of 0° and 90° images of a general structure of interest and that of some known unstrained structure without the need for some reference structure over the same field of view. For this, the projections of reciprocal vectors, unaffected by scan distortions, of the 0° and 90 °images are combined as if they come from a single image. When both displacement and strain tensor with rigid body rotation are of interest, AbStrain-2nd is preferable. To be able to correct for scan distortions, a known *arbitrary* structure must be present beneath or above the zone of interest. Alternatively, AbStrain-2nd can be applied for an image of a general structure obtained after Ophus treatment [31] applied to a couple of 0° and 90° images.

We presented also the method, called Relative displacement, which allows for extracting images of sub-structures, when a crystal is made up of two or more types of atoms, and measuring atomic displacements for each sub-structure individually and with reference to each other. In particular, we showed how to measure the relative displacement, without the need to account for image distortions and be familiar with the crystal's structural characteristics, between a barycenter of the cells constituting a first sub-structure and the atoms of a second sub-structure which are located close to

such a barycenter. Such an approach is interesting to apply for complex semiconductors and functional oxides where polarization induced displacement are inquired.

Each step of the mathematical formalism is illustrated with demonstrative examples.

Finally, we demonstrated a successful application of AbStrain-2nd and Relative displacement to a single HR-STEM image of a $BaTiO_3/SrTiO_3$ ferroelectric heterostructure grown on silicon. The methods proposed here extend the range of possible crystalline materials that can be analyzed by the treatment of their HR-(S)TEM images. For example, nanoparticles embedded within different types of matrices, free-standing nanowires, high-angle grain boundaries, multiple stacks of heterostructures of complex oxides and semiconductors, anti-phase domains and defects inducing long range displacements, constitute just a part of the list of such materials.

ACKNOWLEDGMENTS

The authors acknowledge the support of the French Agence Nationale de la Recherche (ANR), under reference ANR-19-CE24-0027-01 (FEAT project) and ANR-20-CE24-0008 (BePolar project).

Appendix A

For illustrative purposes, we used HR-TEM images obtained at 200 kV in the SACTEM-Toulouse (Tecnai-FEI) microscope, equipped with image aberration corrector and HR-STEM images obtained in a probe corrected JEOL ARM 200F microscope operated at 200 kV, equipped with a cold field-emission electron gun (CFEG) and a probe aberration corrector (ASCOR) allowing a resolution of 0.7 Å at 200 kV in STEM mode. HAADF images were collected with a 21 mrad probe semi-angle, a detector range of 90–370 mrad and a pixel dwell time of 9.5 µs. Focused Ion Beam (FEI Helios Nanolab 600i) was used to prepare 50 nm thick cross-sectional TEM lamellas using a standard lift-out procedure followed by milling with 30 kV Ga ions and cleanup procedure at 2 kV.

The heterostructure under study, Si (001)/a-SiO_x/$SrTiO_3$ (001)/$BaTiO_3$ (001) consists of a 20 nm-thick $BaTiO_3$ (BTO) film grown on a 4 nm-thick $SrTiO_3$ (STO) buffered Si substrate. Since the demonstration of a commensurate heteroepitaxy of STO on Si [34], STO is the standard template for the successful epitaxial growth of other oxides on Si [8]. Here, both BTO and STO were grown by Molecular Beam Epitaxy using a DCA R450 chamber. From X-ray diffraction ($\theta/2\theta$ scans and ϕ scans), the epitaxial relationship between STO & BTO relatively to Si is: (001) BTO or STO // (001) Si and [100] BTO or STO // [110] Si. The 45° in-plane rotation of the $SrTiO_3$ (and subsequently $BaTiO_3$) crystal cells relatively to the Si ones is due to the lattice mismatch between the perovskite structure and the Si one.

References

1. N. Cherkashin, C. Bonafos, H. Coffin, M. Carrada, S. Schamm, G. Ben Assayag, D. Chassaing, P. Dimitrakis, P. Normand, M. Perego, M. Fanciulli, T. Muller, K. H. Heinig, A. Claverie, Fabrication of nanocrystal memories by ultra-low energy ion implantation, Phys. Status Solidi (c) 6 (2005) 1907-1911.
2. A. Kanjilal, J. L. Hansen, P. Gaiduk, A. N. Larsen, N. Cherkashin, A. Claverie, P. Normand, E. Kapelanakis, D. Skarlatos, D. Tsoukalas, Structural and electrical properties of silicon dioxide layers

with embedded germanium nanocrystals grown by molecular beam epitaxy, Appl. Phys. Lett. 82 (8) (2003) 1212-1214.

3. C. Bonafos, L. Khomenkhova, F. Gourbilleau, E. Talbot, A. Slaoui, M. Carrada, S. Schamm-Chardon, P. Dimitrakis, P. Normand, Nano-Composite MOx Materials for NVMs, In Metal Oxides for Non-volatile Memory, Elsevier (2022) 201–244.
4. M. Bayle, C. Bonafos, P. Benzo, G. Benassayag, B. Pécassou, L. Khomenkova, F. Gourbilleau, R. Carles, Ag doped silicon nitride nanocomposites for embedded plasmonics, Appl. Phys. Lett. 107 (2015) 101907.
5. N. A. Bert, V. V. Chaldyshev, N. A. Cherkashin, V. N. Nevedomskiy, V. V. Preobrazhenskii, M. A. Putyato, B. R. Semyagin, V. I. Ushanov, M. A. Yagovkina, Metallic AsSb nanoinclusions strongly enriched by Sb in AlGaAsSb metamaterial, J. of Appl. Phys. 125 (2019) 145106.
6. N. Cherkashin, S. Reboh, M. J. Hÿtch, A. Claverie, V. V. Preobrazhenskii, M. A. Putyato, B. R. Semyagin, V. V. Chaldyshev, Determination of stress, strain, and elemental distribution within In(Ga)As quantum dots embedded in GaAs using advanced transmission electron microscopy, Appl. Phys. Lett. 102 (2013) 173115.
7. A. N. Kosarev, V. V. Chaldyshev, and N. Cherkashin, Experimentally-Verified Modeling of InGaAs Quantum Dots, Nanomaterials, MDPI, 12 (12) (2022) 1967.
8. L. Mazet, S. M. Yang, S. V. Kalinin, S. Schamm-Chardon, C. Dubourdieu, A review of molecular beam epitaxy of ferroelectric $BaTiO_3$ films on Si, Ge and GaAs substrates and their applications, Sci. Technol. Adv. Mater. 16 (3) (2015) 036005.
9. A. A. Demkov, P. Ponath, K. Fredrickson, A. B. Posadas, M. D. McDaniel, T. Q. Ngo, J. G. Ekerdt, Integrated Films of Transition Metal Oxides for Information Technology. Microelectron. Eng. *147* (2015) 285–289.
10. C. Dubourdieu, J. Bruley, T.M. Arruda, A. Posadas, J. Jordan-Sweet, M.M. Frank, E. Cartier, D.J. Frank, S. Kalinin, A. Demkov and V. Narayanan, Switching of ferroelectric polarization in epitaxial $BaTiO_3$ films on silicon without a conducting bottom electrode, Nature Nanotechnology 8 (2013), 748-754.
11. M. Dawber, J. F. Scott, Physics of Thin-Film Ferroelectric Oxides, Reviews of Modern Physics 77 (4) (2005) 1083–1130.
12. L. Baudry, I. A. Luk'yanchuk, A. Razumnaya, Dynamics of Field-Induced Polarization Reversal in Thin Strained Perovskite Ferroelectric Films with c -Oriented Polarization, Phys. Rev. B 91 (14) (2015) 144110.
13. S. P. Beckman, X. Wang, K. M. Rabe, D. Vanderbilt, Ideal Barriers to Polarization Reversal and Domain-Wall Motion in Strained Ferroelectric Thin Films. Phys. Rev. B 79 (14) (2009) 144124.
14. D. P. Kumah, J. W. Reiner, Y. Segal, A. M. Kolpak, Z. Zhang, D. Su, Y. Zhu, M. S. Sawicki, C. C. Broadbridge, C. H. Ahn, F. J. Walker, The Atomic Structure and Polarization of Strained $SrTiO_3$/Si. Appl. Phys. Lett. 97 (25) (2010) 251902.
15. J. Shi, I. Grinberg, X. Wang, A. M. Rappe, Atomic Sub-lattice Decomposition of Piezoelectric Response in Tetragonal $PbTiO_3$, $BatiO_3$, and $KNbO_3$, Phys. Rev. B 89 (9) (2014) 094105.
16. R. Bierwolf, M.Hohenstein, F.Phillipp, O.Brandt, G.E.Crook, K.Ploog, Direct measurement of local lattice distortions in strained layer structures by HREM, Ultramicroscopy 49 (1–4) (1993) 273-285.
17. M. J. Hÿtch; E. Snoeck, R. Kilaas, Quantitative Measurement of Displacement and Strain Fields from HREM Micrographs, Ultramicroscopy 74 (3) (1998) 131–146.

18. P. L. Galindo, S. Kret, A. M. Sanchez, J. Y. Laval, A. Yáñez, J. Pizarro, E. Guerrero, T. Ben, S. I. Molina, The Peak Pairs Algorithm for Strain Mapping from HRTEM Images, Ultramicroscopy 107 (12) (2007) 1186–1193.

19. M. Nord, P.E. Vullum, I. MacLaren, T. Tybell, R. Holmestad, Atomap: a new software tool for the automated analysis of atomic resolution images using two-dimensional gaussian fitting, Adv. Struct. Chem. imaging 3(1) (2017) 9.

20. A. de Backer, K. Van den Bos, W. Van den Broek, J. Sijbers, S. Van Aert, StatSTEM: an efficient approach for accurate and precise model-based quantification of atomic resolution electron microscopy images, Ultramicroscopy 171 (2016) 104–116.

21. Y. Wang, U. Salzberger, W. Sigle, Y. E. Suyolcu, P. A. Van Aken, Oxygen octahedra picker: a software tool to extract quantitative information from STEM images, Ultramicroscopy 168 (2016) 46–52.

22. D. Mukherjee, L. Miao, G. Stone, N. Alem, Mpfit: a robust method for fitting atomic resolution images with multiple Gaussian peaks, Advanced Structural and Chemical Imaging 6 (2020).

23. B. Berkels, High Precision STEM Imaging by Non-Rigid Alignment and Averaging of a Series of Short Exposures, Microsc. Microanal. 18 (2) (2012) 300–301.

24. L. Jones, H. Yang, T. J. Pennycook, M. S. J. Marshall, S. Van Aert, N. D. Browning, M. R. Castell & P. D. Nellist, Smart Align—a new tool for robust non-rigid registration of scanning microscope data, Advanced Structural and Chemical Imaging 1 (8) (2015).

25. N. Cherkashin, M. J. Hÿ˙tch, E. Snoeck, A. Claverie, J. M. Hartmann, Y. Bogumilowicz, Quantitative strain and stress measurements in Ge/Si dual channels grown on a $Si_{0.5}Ge_{0.5}$ virtual substrate, Mater. Sci. Eng. B 124 –125 (2005) 118.

26. N. Cherkashin, M.J. Hÿtch, E. Snoeck, F. Hüe, J.M. Hartmann, Y. Bogumilowicz, A. Claverie, Quantitative local strain measurements in compressive strained Ge/tensile strained Si bi-layers grown on top of relaxed Si0.5Ge0.5 virtual substrates, NIMB 253 (1-2) (2006) 145-148.

27. F. Hüe, M. Hÿtch, H. Bender, F. Houdellier, Al. Claverie, Direct Mapping of Strain in a Strained Silicon Transistor by High-Resolution Electron Microscopy, Phys. Rev. Lett. 100 (2008) 156602.

28. F. Hüe, C. L. Johnson, S. Lartigue-Korinek, G. Wang, P. R., Buseck, M. J. Hÿ˙tch, Calibration of projector lens distortions, J. Electron Microsc. 54 (2005) 181.

29. M. A. Luong, N. Cherkashin, B. Pecassou, A. Claverie, Effect of Nitrogen Doping on the Crystallization Kinetics of Ge2Sb2Te5, Nanomaterials 11 (2021) 1729.

30. H. S. Von Harrach, Instrumental Factors in High-Resolution FEG STEM, Ultramicroscopy 58 (1) (1995) 1–5.

31. C. Ophus, J. Ciston, C. T. Nelson, C. T., Correcting Nonlinear Drift Distortion of Scanning Probe and Scanning Transmission Electron Microscopies from Image Pairs with Orthogonal Scan Directions, Ultramicroscopy 162 (2016) 1–9.

32. A. Louiset, S. Schamm-Chardon, O. Kononchuk, N. Cherkashin, Reconstruction of depth resolved strain tensor in off-axis single crystals: Application to H^+ ions implanted $LiTaO_3$, Appl. Phys. Lett. 118 (8) (2021) 082903.

33. N. Bert, V. Chaldyshev, N. Cherkashin, V. Nevedomskiy, V. Preobrazhenskii, M. A. Putyato, B. R. Semyagin, V. I. Ushanov, M. A. Yagovkina, Sb-rich nanoinclusions in an AlGaAsSb metamaterial, MRS Advances 4 (2019) 277-284.

34. R. McKee, F. Walker, M. Chisholm, Crystalline Oxides on Silicon: The First Five Monolayers, Phys. Rev. Lett. 81 (14) (1998) 3014–3017.